Preprint for **Effect of chemical disequilibrium during metal-silicate partitioning on the thermal state of the early core and implications on the dynamics of metal/silicate segregation**

Authors: Vincent Clesi[1,2] and Renaud Deguen[2,3]

[1]Insitut für Mineralogie, Münster Universität, Correnstraße 24, 48149 Münster

[2]Univ Lyon, ENSL, UCBL, UJM, CNRS, LGL-TPE, F-69007 Lyon, France

[3]Univ. Grenoble Alpes, Univ. Savoie Mont Blanc, CNRS, IRD, Univ. Gustave Eiffel, ISTerre,

38000 Grenoble, France

This preprint is a working document for a paper in preparation by Vincent Clesi and Renaud Deguen.

The working title is “Effect of chemical disequilibrium during metal-silicate partitioning on the thermal state of the early core and implications on the dynamics of metal/silicate segregation”

This is the first version of the paper, including main text, references and supplementary figures.

This article has not been submitted to a peer review journal yet. Several modifications will be made before submission and review.

Effect of chemical disequilibrium during metal-silicate partitioning on the thermal state of the early core and implications on the dynamics of metal/silicate segregation

Vincent Clesi[1,2] **and Renaud Deguen**[2,3]

[1]**Insitut für Mineralogie, Münster Universität, Corrensstraße 24, 48149 Münster**
[2]**Univ Lyon, ENSL, UCBL, UJM, CNRS, LGL-TPE, F-69007 Lyon, France**
[3]**Univ. Grenoble Alpes, Univ. Savoie Mont Blanc, CNRS, IRD, Univ. Gustave Eiffel, ISTerre, 38000 Grenoble, France**

ABSTRACT

In this study, we improved a previously published numerical model linking the core composition to the core temperature during accretion by introducing some amount of chemical disequilibrium during the segregation of the core in the magma ocean phase. At the minimum equilibrium rate in metal and silicate phases, the final temperature of the core by $\sim$ 250 K compared to the fully equilibrated case. The chemical disequilibrium could be then one factor favoring the hot core hypothesis, but has to be coupled with other phenomena (gravitational energy dissipation, radiogenic heat production) to produce a hot core. Furthermore, we combined our model outputs with a previously published parameterization linking the Reynolds number and the equilibrium rate of Ni and Co at the end of accretion. We then showed that if one consider large diapirs (100 - 1000 km radius) of metal equilibrating with the magma ocean, then the only way to obtain a bulk silicate Earth composition is to consider the magma ocean to have high viscosity (10^8 to 10^{15} Pa.s). These results imply that at the end of accretion, the existence of a fully molten, only liquid, magma ocean is highly unlikely; with the reality being closer to a mushy magma ocean with some degree of crystallization equilibrating with large diapirs.

Keywords: Accretion model, Core temperature, metal silicate partitioning, magma ocean, viscosity

1 INTRODUCTION

The presence of light element in the core has been demonstrated for a long time (Birch, 1965), and constraining the nature and concentrations of these light elements is important to understand the so-called core density deficit (Dziewonski and Anderson, 1981). The incorporation of light elements in the core has been proposed to happen in a deep magma ocean, where the core-forming metal segregates from the silicate (e.g. Drake and Righter, 2002; Bouhifd and Jephcoat, 2011). This formation at high pressure and high temperature favors the incorporation of light elements in the core, the main light elements being Si and O (Rubie et al., 2015; Fischer et al., 2017; Clesi and Deguen, 2023; Pu et al., 2025). The final composition of the core, and in particular the concentrations of light elements, is dependent on several factors, the main factors being the composition of the building blocks and the P-T-f_{O_2} conditions of metal-silicate segregation in a deep magma ocean. Among those conditions, the efficiency of mixing in the magma ocean and the degree of chemical equilibrium is often overlooked, with a majority of models focusing on the end-member with full equilibrium (e.g. Wood et al., 2008; Siebert et al., 2012; Fischer et al., 2015, 2017; Clesi et al., 2016; Clesi and Deguen, 2023; Loroch et al., 2024; Pu et al., 2025). The effect of disequilibrium is complex to apprehend, as two phases are involved (e.g. Rubie et al., 2003; Ulvrová et al., 2011; Gu et al., 2023) with dynamic separation of the two phases that are complex to model (e.g. Samuel, 2012; Deguen et al., 2014; Landeau et al., 2021) with elemental specific equilibrium rates (Clesi et al., 2020). In a previous work (Clesi and Deguen, 2023), we used an accretion model combining the metal-silicate partitioning behavior of different elements and a thermal evolution model of the metallic phase, dependent on the metallic phase composition, to link the thermal evolution of the

core to its composition. This model tended to favor the cold core hypothesis (Nomura et al., 2014; Zhang et al., 2016; Dobrosavljevic et al., 2022), particularly if the amount of gravitational dissipation energy going to the metal is low (Monteux et al., 2009; Samuel et al., 2010). The hot core hypothesis (King and Olson, 2011; Andrault et al., 2017; Driscoll and Davies, 2023), to be true, necessitates other mechanisms than the simple compressional heating used in Clesi and Deguen (2023). One mechanism that could increase the initial core temperature is the chemical disequilibrium during the metal-silicate segregation process. Indeed, to explain the bulk silicate Earth composition while considering chemical disequilibrium during core mantle segregation, it is necessary to increase the average depth of the magma ocean (Rubie et al., 2003, 2011; Gu et al., 2023). Clesi and Deguen (2023) showed that such an increase in average magma ocean depth translates into higher core temperatures as well as higher concentrations of Si and O. Therefore, in this study, we modified the model of Clesi and Deguen (2023) by introducing various degrees of disequilibrium in the metallic and silicate phase during the accretion process. We used the results to quantify the effect of chemical disequilibrium on the initial core temperature. Furthermore, we used the outputs of the model combined with the disequilibrium parameterization in Clesi et al. (2020), and showed that, at least at the end of accretion, the magma ocean viscosity cannot be modeled with the viscosity of ultramafic melts.

2 DESCRIPTION OF THE THERMAL MODEL

To determine the heat content and temperature of the core we consider the following steps :

(i) The initial temperature of each addition of metal is set at the bottom of the magma ocean, where the metal is assumed to equillibrate with the silicates. The initial temperature is therefore given by the liquidus of silicate at the pressure of the bottom of the magma ocean, as given by Andrault et al. (2011).

(ii) The metal is then heated by compression while migrating from the bottom of the magma ocean to the growing core. At each step of accretion its composition is different, and we do not consider any mixing, thus resulting in the formation of a stratified core (as in Jacobson et al. (2017)).

(iii) The metal is further heated by compression due to the growth of the core up to its final size. We use the resulting temperature and density profiles to calculate the heat content of the core.

(iv) We assume that the core is then mixed from the stratified state, and use the previously calculated heat content to get the temperature at the CMB (T^{is}_{CMB}) assuming the core to be isentropic. That the core is mixed at the end of accretion is a somewhat strong assumption (Jacobson et al., 2017), but it has the advantage of allowing to quantity the thermal state of the core with a single parameter (here the CMB temperature), which greatly simplifies the analysis.

The details on the model and the different calculations are described in Clesi and Deguen (2023), but we propose a quick description of the thermal model in the following paragraphs.

The initial temperature of the metal is set to be the liquidus temperature of the silicate (Andrault et al., 2011) at the bottom of the magma ocean where the chemical equilibrium happens. It is given by:

$$T_{eq} = 1940 \left(\frac{P_{eq}}{29} + 1 \right)^{1/1.9}, \tag{1}$$

where P_{eq} and T_{eq} are the equilibrium pressure and temperature at the base of the magma ocean. The temperature changes in steps (ii) and (iii) are obtained from:

$$\frac{dT}{T} = \frac{\gamma}{K_s} dP, \tag{2}$$

where γ and K_s are the Gruneisen parameter and isentropic bulk modulus. We use the Murnaghan approximation for the bulk modulus,

$$K_s = K_0 + K' P, \tag{3}$$

with $K_0 = 128.49$, and $K' = 3.67$, which yields the following equation of state for the metal:

$$\frac{\rho(P)}{\rho_0} = \left(1 + \frac{K'}{K_0} P\right)^{1/K'}, \tag{4}$$

where ρ denotes density. The value of ρ_0 is varying throughout accretion, depending on the chemical equilibrium (see Clesi and Deguen (2023) for the details). Following the study of Clesi and Deguen (2023), we used the formalism of Al'Tshuler et al. (1987) for the calculation of the Grüneisen parameter γ given by:

$$\gamma = \gamma_\infty + (\gamma_0 - \gamma_\infty) \left(\frac{\rho_0}{\rho}\right)^\beta, \tag{5}$$

where $\beta = \gamma_0/(\gamma_0 - \gamma_\infty)$, with $\gamma_0 = 1.933$ and $\gamma_\infty = 0.916$ as refitted in Clesi and Deguen (2024b). These values might not be appropriate to get a precise estimate of the core temperature, but the formalism chosen tends to limit the error introduced by the uncertainty on γ_0 and γ_∞ (Clesi and Deguen, 2024b). Nonetheless, the goal of the study is not to determine the precise temperature of the core, but to assess the sensitivity of the thermal model to a specific chemical phenomenon, in this specific instance the dilution and disequilibrium during core/mantle segregation. With this Grüneisen formalism, integrating Equation 2 yields:

$$\begin{aligned} T(P) = T_{eq} \left(\frac{K_0 + K'P}{K_0 + K'P_{eq}}\right)^{\frac{\gamma_\infty}{K'}} \\ \times \exp\left[\frac{\gamma_{0,j} - \gamma_\infty}{\beta} \left(\left(1 + \frac{K'P_{eq}}{K_0}\right)^{-\frac{\beta}{K'}} - \left(1 + \frac{K'P}{K_0}\right)^{-\frac{\beta}{K'}}\right)\right]. \end{aligned} \tag{6}$$

The heat content of the core is then calculated as

$$Q = 4\pi \int_0^{R_{core}} \rho(r) C_p T(r) r^2 dr, \tag{7}$$

where R_{core} is the radius of the core, r the distance from the center of the core, and C_p the specific heat capacity of the metal. The the link between the radius of the core and pressure $P_{core}(r)$ within the core is given by:

$$P_{core}(r) = P_{center} + \left(\frac{P_{CMB} - P_{center}}{R_{core}^2}\right) r^2, \tag{8}$$

where P_{center} and P_{CMB} denote pressure at the center of the core and CMB. The isentropic temperature profile can then be obtained by integrating

$$\left(\frac{\partial \ln T^{is}}{\partial \ln \rho_{core}}\right)_s = \gamma. \tag{9}$$

where γ is the Grüneisen parameter given in Equation 5. In the final step of calculation we consider a fully mixed core with a constant heat content, which allow us to calculate the temperature at the CMB following:

$$T_{CMB}^{is} = \frac{Q}{4\pi \int_0^{R_c} \rho^{is}(r) C_p T^{is}(r) r^2 dr}, \tag{10}$$

which is evaluated numerically. In the following sections, we will evaluate how T_{CMB}^{is} evolves when applying a chemical disequilibrium at stage (i) of the model, thus changing the composition and density profile of the core.

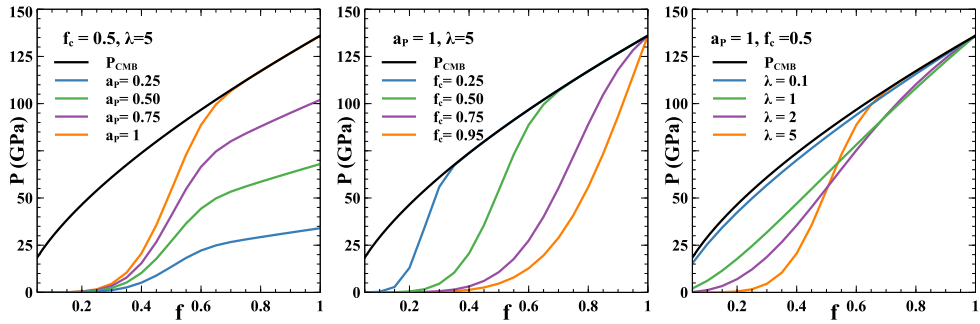

Figure 1. Description of the effect of the parameters used in Equation 11 on the value of P_{eq}. The black line is the pressure at the CMB, $P_{\mathrm{CMB}}(f)$. The left panel shows of P_{eq} with $f_c = 0.5$ and $\lambda = 5$ with variable a_P. The middle panel shows the evolution of P_{eq} for $a_P = 1$ and $\lambda = 5$ with variable f_c. The right panel shows the effect of P_{eq} for $a_P = 1$ and $f_c = 0.5$ with λ variable.

3 DESCRIPTION OF THE CHEMICAL MODEL

The thermal model described above is linked to a chemical model of core/mantle segregation. In this section, we present briefly the initial model used in Clesi and Deguen (2023), and the modifications made to it so as to model a chemical disequilibrium during core/mantle segregation.

3.1 Inputs of the models

We tested a whole range of metal-silicate segregation scenario during accretion. In all of the models presented below, the initial conditions of core-mantle segregation are fixed by the pressure of equilibrium, representing the bottom of the magma ocean. The pressure of equilibrium, P_{eq} is given by:

$$P_{\mathrm{eq}}(f) = a_P P_{\mathrm{CMB}}(f) \frac{1 - \mathrm{e}^{-(f/f_c)^{\lambda}}}{1 - \mathrm{e}^{-(1/f_c)^{\lambda}}}, \tag{11}$$

where f is the mass fraction of the Earth accreted, $P_{\mathrm{CMB}}(f)$ is the pressure at the CMB for a given mass fraction accreted and the parameters a_P, f_c and λ are the varying parameters.

The effect of each parameter on the evolution of the equilibrium pressure P_{eq} is shown in Figure 1. As shown in the left panel of Figure 1, a_P is the parameter controlling the maximum pressure at the end of accretion, and is a fraction of the final value of $P_{\mathrm{CMB}}(f)$, varying between 0.05 and 1. Depending on the values of f_c and λ the maximum pressure is reached sooner or later during the accretion, but the maximum is set by a_P. For $a_P = 1$, the value of P_{eq} reach the same value as the pressure at the CMB, for $a_P = 0.5$, P_{eq} will always be lower or equal to half of the CMB pressure at any point of accretion. In the middle panel of Figure 1, we show the effect of the scale parameter f_c on the evolution of the pressure of equilibrium. This parameter sets the moment in accretion when the pressure increases faster, especially for high values of λ. It is also when we chose to change the oxidation state of the impactor, and therefore the initial composition of metal and silicate accreted, from a reduced composition to an oxidized composition (see below and Table 1). Finally, the right panel of Figure 1 we show the effect of the shape parameter λ on P_{eq}, determining the shape of the accretion profile. When $\lambda = 0$, Equation 11 becomes $P_{eq}(f) = a_P P_{\mathrm{CMB}}(f)$, i.e. the magma ocean depth is a fixed fraction of the CMB depth all along the accretion, as it is classical in several other studies (Wood et al., 2008; Siebert et al., 2012; Bouhifd et al., 2007; Clesi et al., 2016). When $\lambda \to \infty$, the Equation 11 becomes a step function with $P_{eq}(f) = 0$ for $f < f_c$ and $P_{eq}(f) = a_P P_{\mathrm{CMB}}(f)$ for $f > f_c$. As can be seen in Figure 1, using a finite value of λ, varying between 0.1 and 5 in this study, smooth out the step function, and the transition to a shallow (i.e. low P_{eq}) to a relatively deep magma ocean (i.e. P_{eq} close to the maximum pressure allowed by a_P value).

The scale parameter f_c does not only control the transition of regime for high values of λ, but also the composition of the impacting masses. We chose a simple model of having only two different initial compositions: one reduced and one oxidized. The compositions, taken from Fischer et al. (2015), exhibit CI-chondritic elemental ratios (Wasson and Kallemeyn, 1988) in order to match the refractory lithophile element trend in the Bulk Silicate Earth (McDonough and Sun, 1995). For $f < f_c$, the Earth is accreting the reduced composition presented in Table 1, and for $f > f_c$ the Earth is accreting the oxidized

Elements	Reduced material	Oxidized material
Silicate phase		
SiO_2	51.41	42.19
MgO	37.5	29.40
Al_2O_3	4.62	3.63
CaO	3.75	2.95
FeO	2.24	21.13
NiO (ppm)	10.1	174
CoO (ppm)	5.1	83
Cr_2O_3 (ppm)	4500	6170
V_2O_3 (ppm)	203	164
Metallic phase		
Fe	91.1	89.07
Ni	5.55	10.0
Co	0.26	0.34
Si	2.4	0.0205
Cr (ppm)	6100	870
V (ppm)	9.24	0.775
O	0.04	0.4
Metallic mass fraction of the impactor		
-	0.313	0.165

Table 1. Impactor composition given in Fischer et al. (2015) supplementary material and used in our model. All units are in wt % except where ppm is specified.

composition presented in Table 1. Accreting reduced material before oxidized material is consistent with N-body simulations of Solar System formation that tend to accrete inner solar system material material (hotter, more reduced and less rich in volatile elements) first and outer solar system material (cooler, more oxidized and rich in volatile elements) at the end of accretion (Morbidelli et al., 2000; Raymond et al., 2009; Izidoro et al., 2021). The parameters and compositions presented in this section are used in all of the models presented in the following subsections, and a schematics of the physical meaning of the model, derived from Clesi and Deguen (2024a), is given in supplementary Figure S1.

3.2 Reference chemical model description

The core-mantle segregation model we will take as a reference for this study is based on the work of Fischer et al. (2015), with the link to the thermal model being explained in Clesi and Deguen (2023). A qualitative description of the model is given in Figure 2. The model consists on the following steps of calculations:

i Initialisation of the calculation: we accrete a planetesimal corresponding to 5 % of the Earth mass, and calculate the initial core and mantle composition by equilibrating the entire mass of the metal and silicate at a given pressure. This equate to a single stage model for the first 5% of accretion, which is standard for small bodies (e.g. Grewal et al., 2019, and references therein)

ii Main accretion process: the Earth is growing by adding impactor of 5% of the Earth size. All of the metal in the impactor mass and only the impactor silicate mass are re-equilbrated at the bottom of the magma ocean, which set the pressure and temperature of equilibrium (P_{eq} and T_{eq}). The metal then sink into the core, adding a chemically different layer on top of the growing core. During the descent, the temperature of the core is increasing from T_{eq} to its final temperature due to compressional heating (of the mantle then the growing core) following Equation 6. It is chemically insulated from the mantle and the other layer of core. Before another impactor is added, the mantle is considred well-mixed. This process continues until the entire Earth mass is accreted.

iii Final stage: at the end of the main process, we get a fully accreted Earth with a stratified core and a well-mixed mantle. We consider that the core is then mixed isentropically to calculate the temperature at the CMB, T^{is}_{CMB}, given by Equation 10.

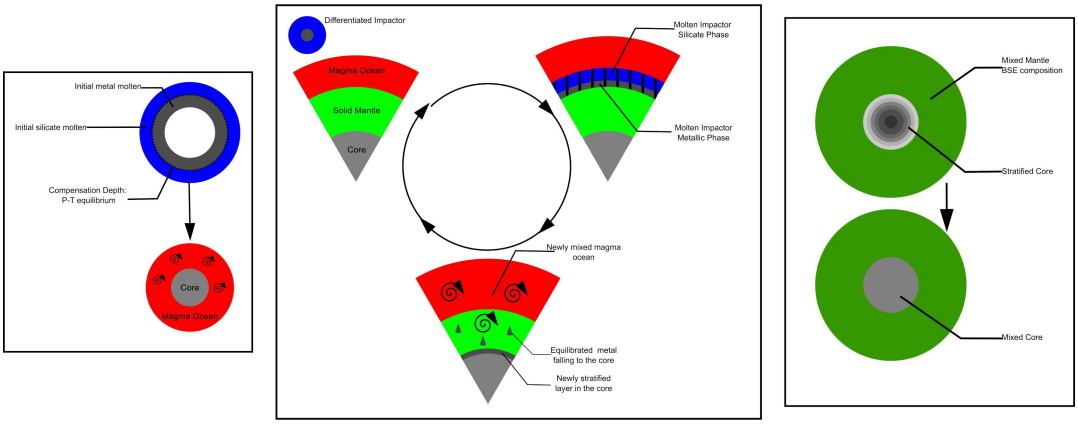

Figure 2. Qualitative description of the model as described in Fischer et al. (2015) and in Section 3.2. The left rectangle described the first step of accretion, setting the initial composition of the planestesimal. The middle rectangle describes the main accretion process: an impactor on a magma ocean is re-equilibrated at the bottom of the magma ocean before segregation of the core and mixing of the whole mantle by vigorous convection. The right rectangle shows the last part of the model: once the mass of the Earth is obtained, we calculate the heat content of a segregated core and calculating the temperature of a mixed core.

At each step, the composition of mantle and core is simplified, and we consider the following equilibrium described by Rubie et al. (2011):

$$\begin{gathered}\left[(FeO)_x(NiO)_y(SiO_2)_z(Al_uCa_mMg_p)O + Fe_aNi_bO_cSi_d\right] \\ \updownarrow \\ \left[(FeO)_{x'}(NiO)_{y'}(SiO_2)_{z'}(Al_uCa_mMg_p)O + Fe_{a'}Ni_{b'}O_{c'}Si_{d'}\right]\end{gathered} \tag{12}$$

The equilibrium of Reaction 12 is described by sub-reactions for each element involved, following:

$$MO^{m.o.}_{n/2} + \frac{n}{2}Fe^m \rightarrow M^m + \frac{n}{2}FeO^{m.o.}, \tag{13}$$

where $MO^{m.o.}_{n/2}$ is a given element of valence n in oxide form in the magma oceanphase, and M^m the metallic form of the element in the metallic alloy. The equilibrium of each sub-reaction is set by the exchange partitioning coefficient K_d, which is parameterized by:

$$log_{10}K_d^M = a_M + \frac{b_M}{T_{\text{eq}}} + \frac{c_M P_{\text{eq}}}{T_{\text{eq}}}, \tag{14}$$

where P_{eq} is expressed in GPa, T_{eq} in K. The coefficients (a_M, b_M and c_M) of equation 14 for each element are the one given in Fischer et al. (2015). For a given element the exchange partitioning coefficient is by definition:

$$K_d^M = \frac{\chi_M^m}{\chi_{MO_{n/2}}^{m.o.}} \left(\frac{\chi_{FeO}^{m.o.}}{\chi_{Fe}^m}\right)^{n/2}, \tag{15}$$

with χ_M^m the molar fraction of element M in the metallic phase, and $\chi_{MO_{n/2}}^{m.o.}$ the molar fraction of the corresponding oxide in the silicate. Combining Equation 12 and equation 15 with the K_d^M value set by equation 14 allows to calculate the final equilibrated composition of both phases with a self-evolving oxygen fugacity for most of the elements. The partitioning of V, Cr and Co are also calculated after the

initial equilibrium of reaction 12 using the same method. The main calculation consist in solving the mass balance system of equations:

$$\begin{array}{lcl} x+a & = & x'+a' \\ y+b & = & y'+b' \\ z+d & = & z'+d' \\ x+y+2z+u+m+p+c & = & x'+y'+2z'+u+m+p+c' \end{array} \tag{16}$$

with a, b, c, d, u, m, p, x, y, z, a', b', c', d', x', y', z' the number of moles of the elements involved in reaction 13. This system of equation is combined with the one created by the K_d of Ni, Si and O, with Equation 15 applied for each element. For instance for Ni, an element with a valence of 2, expressing Equation 15 becomes:

$$K_d^{Ni} = \frac{b'}{a'+b'+c'+d'} \times \frac{x'+y'+z'+u+m+p}{y'} \times \left(\frac{x'}{x'+y'+z'+u+m+p} \times \frac{a'+b'+d'}{a'} \right)^{2/2} \tag{17}$$

Combining system 16 with 17 for Ni, Si and O yield a system of 7 equations with 7 unknown (a', b', c', d', x', y', z') that allows for several solution, only one respecting the fact that no mass can be negative. The complexity is the formula of K_d^O, which is calculated using the formula given in Frost et al. (2010). The valence 3+ elements (V and Cr) are solved after the main calculation, because the system would become harder to solve analytically. It introduces an error in the masses of silicate and metal, but it is limited to a variation of 0.01 to 0.1 %. The detailed method of for solving the system of equation calculation is described in the supplementary information of Rubie et al. (2011) and Clesi and Deguen (2023). The number of moles involved in the initial stage of the reaction is calculated using the mass and composition of the silicate and metal involved in the metal-silicate reaction 12. In the case of the reference model of this study (Fischer et al., 2015; Clesi and Deguen, 2023), the mass of both silicate and metallic phase involved is equal to the silicate and metal in the impactor (Figure 2). The composition of each phase involved is also the composition of the impactors, given in Table 1. The number of mole for element in the metal M is therefore:

$$\mathcal{N}_M^{met} = \frac{m_{metal}^{impactor} X_M^{m,imp}}{\mathcal{M}_M}, \tag{18}$$

where $\mathcal{N}_M^{met}$ is the number of mole of M (a,b,c or d in Reaction 12), $m_{metal}^{impactor}$ is the mass of metal in the impactor, $X_M^{m,imp}$ the mass fraction of element M in the metallic phase of the impactor and $\mathcal{M}_M$ the molar mass of element M. As for the silicate, the number of mole of an oxide $MO_{n/2}$ is given by:

$$\mathcal{N}_{MO_{n/2}}^{sil} = \frac{m_{silicate}^{impactor} w_{MO_{n/2}}^{sil,imp}}{\mathcal{M}_{MO_{n/2}}}, \tag{19}$$

with $\mathcal{N}_{MO_{n/2}}^{sil}$ the number of mole of $MO_{n/2}$ (x, y, z, u, m, p in Reaction 12), $m_{silicate}^{impactor}$ the mass of silicate in the impactor, $w_{MO_{n/2}}^{sil,imp}$ the mass fraction of $MO_{n/2}$ in the silicate phase of the impactor and $\mathcal{M}_{MO_{n/2}}$ the molar mass of oxide $MO_{n/2}$.

Since only the impactors are equilibrated, the bulk composition at a given mass fraction is given by:

$$w_{i,\text{bulk}}^{s+}(f) = \frac{w_i^s(f) m_{\text{accreted}}^s(f) + w_{i,\text{bulk}}^{s-} M_{\text{mantle}}^-}{M_{\text{mantle}}^+}, \tag{20}$$

where $w_{i,\text{bulk}}^{s-}(f)$ and $w_{i,\text{bulk}}^{s+}(f)$ are the bulk concentrations (in % wt) before and after the impact is added, and M_{mantle}^- and M_{mantle}^+ the masses of the mantle before and after the impact ($M_{\text{mantle}}^+ = M_{\text{mantle}}^- + m_{\text{accreted}}^s(f)$). When properly calculated at each step of accretion then for f=1, Equation 20 yields the bulk composition of the mantle. The same equation can be applied to the core, only by replacing the masses of silicate and mantle by the masses of metal and core respectively.

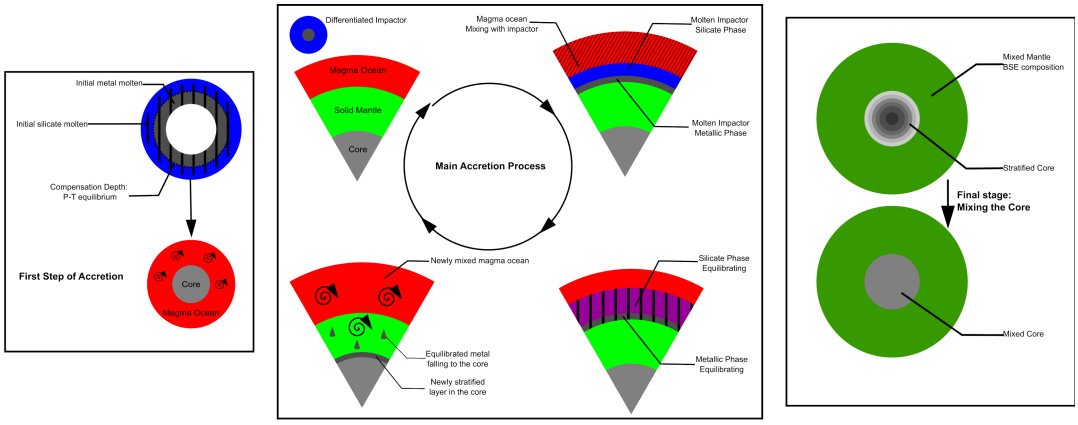

Figure 3. Schematic of the model of disequilibrium used in this study. In all steps only a part of the metal and the silicate is considered to have reacted, even at the first initiation stage. The vertical striped areas represent the amount of metal and silicate reacting. For readability, we considered $k = 1$ (all metal reacted) and an arbitrary value of Δ. Compared to Figure 2, a mixing step has been added before the actual reaction. The amount of silicate equilibrated is colored purple with black stripe in the main accretion stages, and is calculated on the fully mixed magma ocean before reacting with the metal. Once the purple part composition is changed, the magma ocean is fully mixed before the subsequent impact. The last part of the model (re-mixing of the core and mantle) is the same as in the reference model.

3.3 Modeling of disequilibrium

Now that the reference model and the dilution effect are described, we used the calculation technique of Deguen et al. (2014) to model the disequilibrium between the phases. Since the model is not a time-resolved model, the equilibrium rate is approximated by the amount of reacting silicate and reacting metal that are equilibrated. To simplify the calculation of these masses at each step, we considered that the silicate impactor is mixed with the previous mantle before reacting.

We therefore define, following Deguen et al. (2014), two parameters that are used to model this phenomenon: k, a parameter describing the amount of metal that is equilibrated and Δ, the degree of dilution of the metal, i.e. the amount of silicate that is equilibrated. The parameter k is defined by:

$$k = \frac{m_{eq}^{met}}{m_{total}^{met}}; \tag{21}$$

where m_{eq}^{met} is the mass of metal that is equilibrated, and m_{total}^{met} is the total mass of the metal added from the impactor. The parameter Δ is defined by :

$$\Delta = \frac{m_{eq}^{sil}}{m_{eq}^{met}}; \tag{22}$$

where m_{eq}^{sil} is the amount of silicate equilibrated, and m_{eq}^{met} is the amount of metal equilibrated given by equation 21. This way of defining the degree of equilibrium links the amount of equilibrium in the silicate to the amount of equilibrium in the metallic phase, therefore not treating the equilibrium in each phase as independent parameter. Therefore, direct comparison with studies such as Gu et al. (2023) cannot be performed as the amount of silicate equilibrated for a given value of Δ varies first with the value of k (see Equation 22) and varies also within the accretion model (in particular the parameter f_c, see Figure S.3), since the total amount of metal added depends on the moment of accretion, the mass added being lower for the oxidized part of the accretion process (see Section 3.1). For the higher values of Δ ($\sim$ 90 to 100, depending on the value of k), the entire mantle is equilibrated (see Figure S.3 for the actual percentage of mantle equilibrated). We tested the models for k ranging between 0.05 and 1, and for Δ ranging between 1 and 500. The values higher than $\Delta = 100$ are redundant since 99.9 to 100 % of the mantle is equilibrated, but serves as control of the stability of the model.

3.4 Definition of a solution and reference model

As in Clesi and Deguen (2023), we ran 20 000 models of accretions for each (k, Δ) couple. In these 20 000 models, the outputs mantle compositions are not necessary close to the Bulk Silicate Earth (BSE) composition. Therefore, we consider a model given by a (a_P, f_c, λ) triplet to be a solution if all the elemental concentrations are within an acceptable range relatively to the BSE as defined in McDonough and Sun (1995). All major elements concentrations are considered solutions if their values are within a 10 % range of the values of the BSE: $w_{SiO_2}^{mantle} = 45.18 \pm 4.52$ $\%wt$, $w_{Al_2O_3}^{mantle} = 4.47 \pm 0.45$ $\%wt$, $w_{FeO}^{mantle} = 8.10 \pm 0.81$ $\%wt$, $w_{MgO}^{mantle} = 38.03 \pm 3.80$ $\%wt$ and $w_{CaO}^{mantle} = 3.56 \pm 0.36$ $\%wt$. For the trace elements, the concentrations are considered solutions if their values are within 15% of the values of the BSE: $w_{NiO}^{mantle} = 2509 \pm 376$ ppm, $w_{CoO}^{mantle} = 134 \pm 20$ ppm, $w_{V_2O_3}^{mantle} = 121 \pm 18$ ppm and $w_{Cr_2O_3}^{mantle} = 3859 \pm 579$ ppm. A model is considered as a solution only if all the different concentrations fall into the ranges defined above. For this publication, the reference model solutions to which everything will be compared is the model described in Section 3.2 and Figure 2 for which the filter described above has been applied. This differs from the initial publication of Clesi and Deguen (2023) in which we used a weighted method that tend to yields more solutions by allowing some elements concentrations, in particular V and Cr, to be outside the 15% range of the BSE concentration. Overall, the trends highlighted in Clesi and Deguen (2023) (correlation between light elements concentration in the core, core temperature and mean pressure of equilibrium) are the same, with less points (see Figure S.2). Some of the models with high values of $\overline{P_{eq}}$, and therefore higher concentrations of Si and O in the core, are removed from the dataset. A comparison between the solution from Clesi and Deguen (2023) and the reference we use in this study (also used in Clesi and Deguen, 2024a, under the name C20) is presented in Figure S2. This shows that the kind of filter applied to define a solution does affect to some extent the output of the models. Several other filters could have been used for instance using the mean quadratic difference like in Rubie et al. (2015) or using uniquely the N-body simulation results combined with a sensitivity study as in Gu et al. (2023). In any case, the trends we highlighted would yield correlations in the same order of magnitude, as evidenced by the comparison of two methods for selecting a solution provided in Figure S2. For the purpose of this study, this issue will not be discussed further, since we will focus on the effect of disequilibrium with a consistent way of selecting the solutions throughout the entire study.

4 RESULTS OF THE CALCULATIONS

4.1 Number of solutions

For the range of k and Δ tested, the models yield between 0 and 241 solutions. As shown in Figure 4, most of the disequilibrium models do not yield any solution: for any value of k below 0.6 and for any value of Δ below 4, no model will yield a BSE-like mantle. This shows the need to have at least some equilibration in both phases. For dilution factors Δ superior to 100, the number of solutions for a given value of k does not change, indicating that the full mantle is equilibrated during the entire time of accretion (see also Figure S.3). Figure 4 also shows that the maximum number of solutions is not reached for full equilibration of both phases: the optimum is obtained when 70 to 80 % of the metallic mass is equilibrated with a dilution factor between 55 and 100. Higher equilibrium rates in the metal or in the silicate do not increase the number of solutions, and even tend to decrease the number of solutions in the case of the values of k. This indicates that it is easier to model the accretion of the BSE with some moderate disequilibrium in the metal, at least with the chondritic material we used in these models. Finally, the number of solutions drastically decreases for $k < 0.7$ and for $\Delta < 30$. Therefore, while it is easier to produce a BSE mantle with moderate disequilibrium, it is highly improbable to form the Earth with high rate of disequilibrium in the silicate or metallic phase.

4.2 Chemical equilibrium controls on the accretion scenarios

In this section we present how the degree of equilibrium affects the type of model that can yield coherent chemical solutions.

4.2.1 Effect of silicate dilution

On Figure 5 are presented the evolutions of the different input parameter values that yield chemically coherent solutions as a function of the amount of equilibrium in the silicate (Δ) for $k = 0.6$, $k = 0.75$ and $k = 1$. Other plots, in the same fashion but for the other elements composing the mantle and the core, are presented in supplementary Figures S4 to S19. No effect of silicate dilution can be seen on the parameter

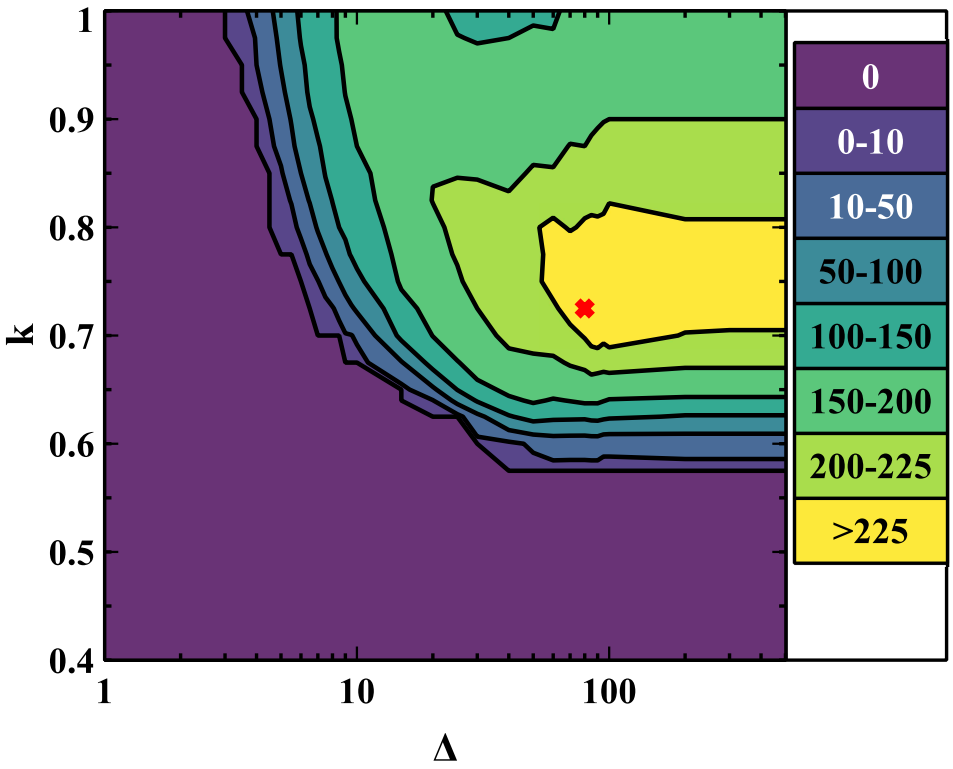

Figure 4. Number of solutions yielded by the model for different values of k (fraction of metal equilibrated, Eq. 21) and Δ (silicate mass equilibrated, see Eq 22). x-axis is in logarithm scale, y-axis in linear scale. The red cross marks the maximum value (n = 241) at k = 0.725 and Δ = 80.

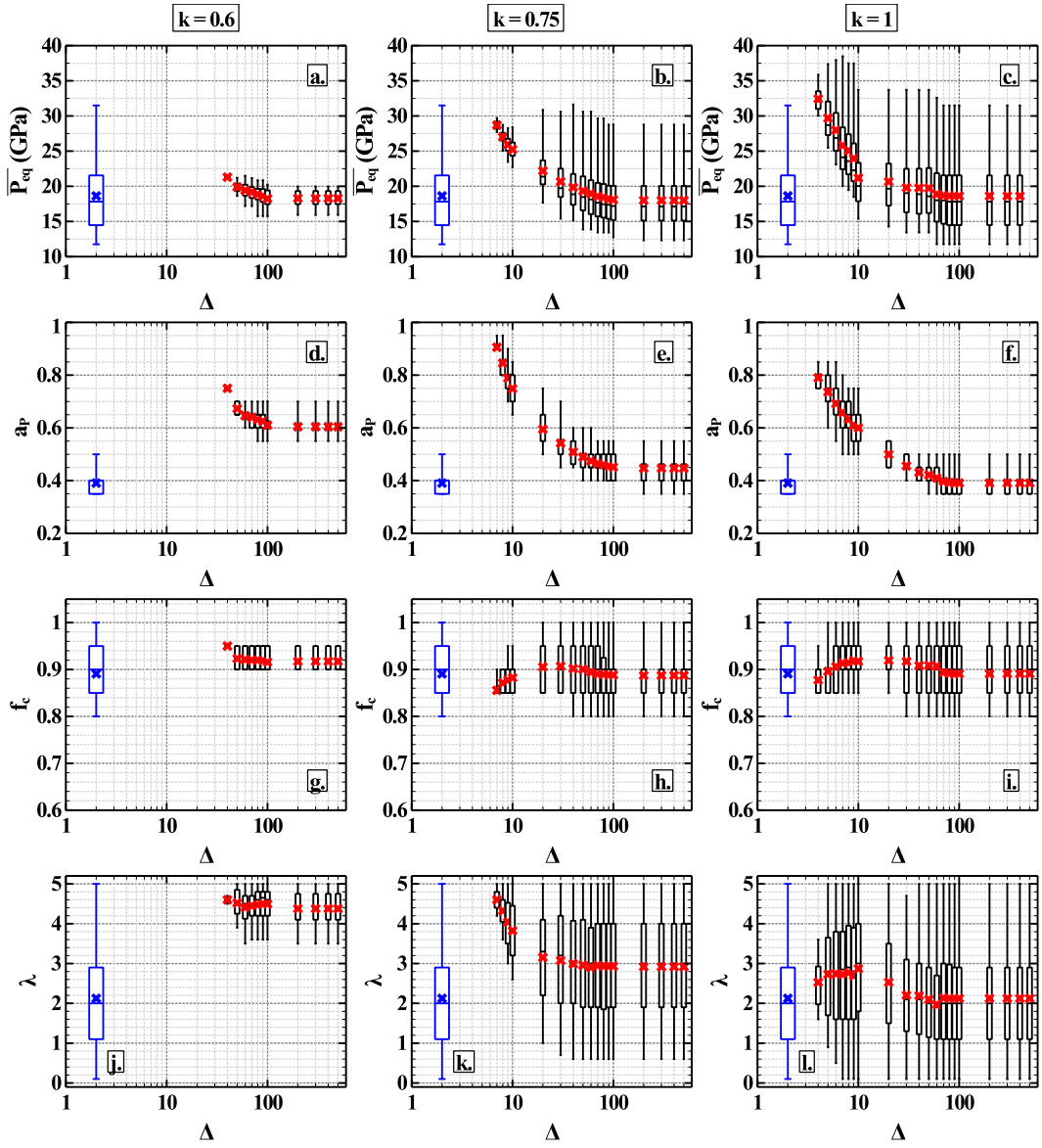

Figure 5. Effect of the silicate dilution Δ on the input parameters controlling the output composition of the model mantle for different values of k. First row, panels a. to c.: $\overline{P_{eq}}$ in GPa. Second row, panels d. to f.: a_P. Third row, panels g. to i.: f_c. Fourth row, panels j. to m.: λ. The left, middle and right column shows the evolution of the parameters values for $k = 0.6$, $k = 0.75$ and $k = 1$, respectively. In each panel the entire solutions range are presented as boxplots, with the red cross being the mean value of the parameter, the white box delimiting the 1st and 3rd quartile, the horizontal line the median value and the vertical lines the minimum and maximum values. The reference model dataset is presented in blue with the same type of plot for comparison.

f_c, which controls the redox state of the impactor: the f_c range is between 0.8 and 1, with mean values close to 0.75 for every model, including the reference model. Therefore, the amount of disequilibrium during core-mantle segregation does not affect the redox state significantly: most of the accretion has to be from reduced impactors (more than 80 %) with the more oxidized impactors arriving at the end. For most of the values of Δ, some models can yield chemically coherent Earth mantles for a fully reduced accretion. However,it is impossible to accrete chemical coherent Earth for a fully reduced accretion at very low values of Δ ($\Delta \sim 4-7$, Figure 5, panels h. and i.). This effect is enhanced for low values of k (Figure 5, panel g.), which indicates it is impossible not to accrete oxidized material if the equilibrium rates in both phases are very low. This effect is common to Δ and k and is discussed further in the following subsection.

The effect of silicate disequilibrium on the type of solution obtained is the same for each value of k: as Δ is lowered, the mean pressure of equilibrium during accretion is increased in order to get chemically coherent solutions. This effect is more visible on panels b. and c. of Figure 5: for $k = 0.75$ and $\Delta = 100$, the mean value of $\overline{P_{eq}}$ is 18 GPa, while for $\Delta = 7$ the mean value of $\overline{P_{eq}}$ is 28 GPa; and for $k = 1$ the mean value of $\overline{P_{eq}}$ varies between 33 GPa and 18 GPa for Δ varying from 4 to 100, respectively.

The parameter a_P, which controls the maximum extent of the magma ocean is likewise increased as Δ decreases: for $k = 1$, the mean value of a_P increases from 0.4 to 0.8 for Δ decreasing from 100 to 4. This mean that when the degree of equilibrium is low, the magma ocean is twice as deep as when the entire magma ocean is equilibrated, thus leading to higher mean pressure of equilibrium during accretion.

The parameter λ, which control the style of accretion (stable depth for magma ocean or sharp transition from shallow to deep magma ocean) is also affected by the silicate dilution imposed on the model. As shown in panels j., k. and l. of Figure 5, the reference model span the entire range of λ values tested, while it is not the case for the disequilibrated model, especially at low values of k and for low values of Δ. Indeed, for $k = 0.75$ the mean value of λ decreases from 4.9 to 3.1 for Δ increasing from 7 to 100. Furthermore, the range of λ value that provides chemically coherent solutions gets narrower as the amount of silicate equilibrated decreases: for $k = 0.6$, the range of λ values is comprised between 3.5 and 5 for all Δ values that yield solutions; for $k = 0.75$, the range varies from 4.2 to 5 for $\Delta = 7$ and from 0.2 to 5 for $\Delta = 100$; and for $k = 1$ the range varies from 1.8 to 3.6 for $\Delta = 4$ and between 0.1 and 5 for $\Delta = 100$. This indicates that when the silicate is not equilibrated, the only scenarios of accretion that can yield chemically coherent Earth analogs are the ones that tend to have very shallow magma oceans during most of their accretion process followed by a dramatic increase of magma ocean depth toward the end of accretion.

4.2.2 Effect of metal equilibrium

In Figure 6 are shown the evolutions of input parameters values as a function of the metallic equilibrium rate k for $\Delta = 10$, $\Delta = 50$ and $\Delta = 100$. Other plots, focusing on the other elements composing the core and mantle, are presented in supplementary Figures S4 to S19.

Like the silicate dilution effect, the disequilibrium of the metallic phase does not change, for the most part, the f_c values, with all ranges of solution between 0.8 and 1, and mean values of f_c around 0.88 for all values of Δ. This means that in order to get chemically consistent Earth's mantle, accretion scenarios need to include at least 80% of reduced material and less than 20 % of oxidized material at the end of accretion, with some solutions possible for 0% of accreted material. A noticeable trend on the value of this parameter is that as the values of k and Δ get lower, the range of f_c values gets narrower. For the lowest values of k and Δ that yields solutions, no solution can be found for 100% reduced accretion. This effect is only valid for the minimum values of k (between 0.6 and 0.7 depending on Δ) and the minimum values of Δ (4 to 7 depending on the value of k). This indicate that very low equilibrium rate during accretion render the accretion of some oxidized material necessary in order to obtain chemically coherent Earth.

As for the parameter λ, k affects the value of λ in the same way as Δ: decreasing the degree of equilibrium tends to select higher values of λ in order to get a solution. For instance, for $\Delta = 50$ (Figure 6, panel k.), the range of λ that yield solutions is comprised between 3.9 and 5 (mean at 4.5) for $k = 0.6$, and is comprised between 0.1 and 5, *i.e.* the entire range of λ values tested, for $k = 1$. This shows that decreasing the amount of metal equilibrated during accretion favor models where the magma ocean is shallow at first, turning into a deep magma ocean dramatically at the end of accretion. More metal and silicate equilibrating tends to favor on the other hand a more steady increase in the magma ocean depth.

The effect of k on $\overline{P_{eq}}$ and a_P is comparable to the effect of Δ: as the amount of metal equilibrated is lowered, the mean pressure of equilibrium is increased in order to get a chemically coherent Earth.

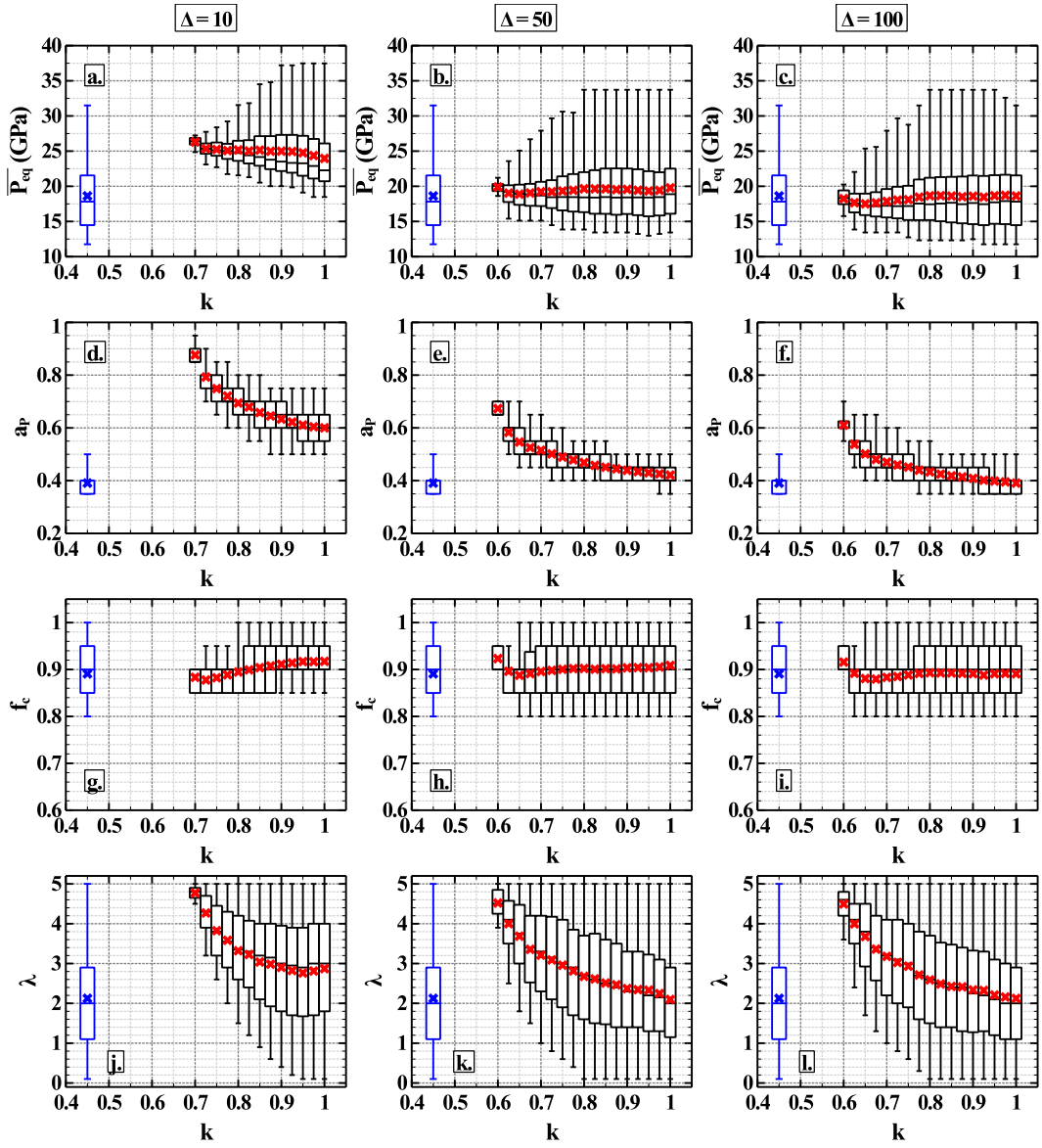

Figure 6. Effect of metal equilibrium k on the input parameters controlling the output composition of the model mantle for different values of Δ. First row, panels a. to c.: $\overline{P_{eq}}$ in GPa. Second row, panels d. to f.: a_P. Third row, panels g. to i.: f_c. Fourth row, panels j. to l.: λ. The left, middle and right column shows the evolution of the parameters values for $\Delta = 10$, $\Delta = 50$ and $\Delta = 100$, respectively. In each panel the entire solutions range are presented as boxplots, with the red cross being the mean value of the parameter, the white box delimiting the 1st and 3rd quartile, the horizontal line the median value and the vertical lines the minimum and maximum values. The reference model dataset is presented in blue with the same type of plot for comparison.

This effect is enhanced by lowering the value of Δ: for $\Delta = 100$ (Figure 6, panel f.), the mean value of a_P decreases from 0.61 to 0.4 when k increases from 0.6 to 1; for $\Delta = 10$ (Figure 6, panel d.), the mean value of a_P decreases from 0.83 to 0.6 when k increases from 0.7 to 1. This effect is comparable to the effect Δ has on a_P. This shows that the maximum extent of the magma ocean at the end of accretion is significantly affected by the degree of equilibrium both in the silicate and metallic phases. However, the clear effect of Δ on the mean pressure of equilibrium during accretion $\overline{P_{eq}}$, shown in the previous section, is less visible, though still present, when plotting the values of $\overline{P_{eq}}$ as a function of k. Indeed, lower k values tend to yield higher mean values (and mostly median values) of $\overline{P_{eq}}$ than higher values of k: for instance for $\Delta = 10$ (Figure 6, panel a., the mean value of $\overline{P_{eq}}$ is 26 GPa for $k = 0.7$and $\overline{P_{eq}} = 24$ GPa (the median value being 22 GPa) for $k = 1$. This effect is not as clear as the effect of k on a_P, because increasing k tends to widen the range of $\overline{P_{eq}}$, in particular because the maximum value of $\overline{P_{eq}}$ increases with increasing k. For instance, for $\Delta = 100$ (Figure 6, panel c.), the maximum value of $\overline{P_{eq}}$ increases from 20 GPa for $k = 0.6$ to 32.6 Gpa for $k = 1$ and reaching a maximum at 33.75 GPa for k between 0.7 and 0.95. This discrepancy in the effect of k on a_P and $\overline{P_{eq}}$ which are highly correlated shows that the degree of metal equilibrium controls more the maximum extent of the magma ocean at the end of accretion (which is the physical meaning of the a_P parameter, Figure S1) than the overall pressure necessary to get a chemically coherent mantle, which is more controlled by the degree of equilibrium in the silicate.

4.3 Chemical equilibrium effect on temperature and core composition

In this section we present how the degree of equilibrium affects the thermal and compositional outputs of the Earth's core.

4.3.1 Effect of silicate dilution

The main output of our model is the composition of the core, in particular the Si and O contents, and the heat content (T^{is}_{CMB}) it correlates with. In Figure 7 are presented the evolution of this three parameters as a function of Δ for $k = 0.6$, $k = 0.75$ and $k = 1$. The more silicate phase equilibrated, the lower the heat content of the core, especially if a large portion of the metal is equilibrated (see panels a. and c. on Figure 7). For instance, when $k = 1$ (panel c., Figure 7), the mean value of T^{is}_{CMB} decreases from 4050 K to 3970 K when Δ increases from 4 to 100. This relates to the effect Δ has on the input parameters: the more the silicate is equilibrated, the lower $\overline{P_{eq}}$ needs to be to yield a chemically coherent mantle, and therefore the temperature of the metal accreted to the core is lower. However, this effect on mean values is low, with a decrease of only 100 K for $k = 1$, and 50 K for $k = 0.6$., between the minimum equilibrium possible and a full magma ocean equilibration. The effect of k, i.e. metal equilibrium, seems to be more important on the heat content and core temperature (see the range of T^{is}_{CMB} on panels a., b. and c. of Figure 7), which is more discussed in the following section.

Because lowering Δ values tend to increases $\overline{P_{eq}}$ during accretion, the output core compositions tend to integrate more light elements as the degree of silicate equilibrium decreases. This is true for both Si and O, with the effect being more important for O than Si. Indeed, the mean values of w^{core}_{Si} for $k = 1$ decreases from 4.8 % wt to 3.9 % wt when Δ increases from 4 to 100 (Figure 7, panel f.); while the mean values of w^{core}_{O} for $k = 1$ (Figure 7, panel i.) decreases from 1.47 to 0.27 % wt when Δ increases from 4 to 100. This shows that the oxygen content of the core is more affected by the mean pressure and type of accretion (higher values of $\overline{P_{eq}}$, a_P and λ for lower Δ, see Figure 5) than Si, despite both reacting the same way to the lack of equilibrium in the silicate phase. Overall, these results show that there is a positive correlation between the heat content and the light elements concentrations in the core that is mediated by the mean pressure of equilibrium during the metal/silicate segregation phase. The mean pressure of equilibrium is inversely proportional to the silicate equilibrium, and therefore decreasing the amount of silicate equilibrated tends to increase both the heat content and light elements content of the core.

4.3.2 Effect of metal equilibrium

The effect of metal equilibrium k on T^{is}_{CMB}, w^{core}_{Si} and w^{core}_{O} for fixed values of Δ (10, 50 and 100) is presented in Figure 8. This figure shows that all the output of the model are less sensitive to the amount of metal equilibrated than the amount of silicate equilibrated (see Figure 7 for comparison). The trends in Figure 8, especially on the mean and median values, are not as clear as the trends that emerges when plotting the same parameteer as a function of Δ. However, one can note that for $\Delta = 10$, increasing k from 0.7 to 1 lead to a decrease of the mean value of w^{core}_{O} from 0.97 to 0.65 % wt (Figure 8, panel g.). This decrease is less important than the one observed when varying Δ for $k = 1$ (Figure 7, panel j.), thus

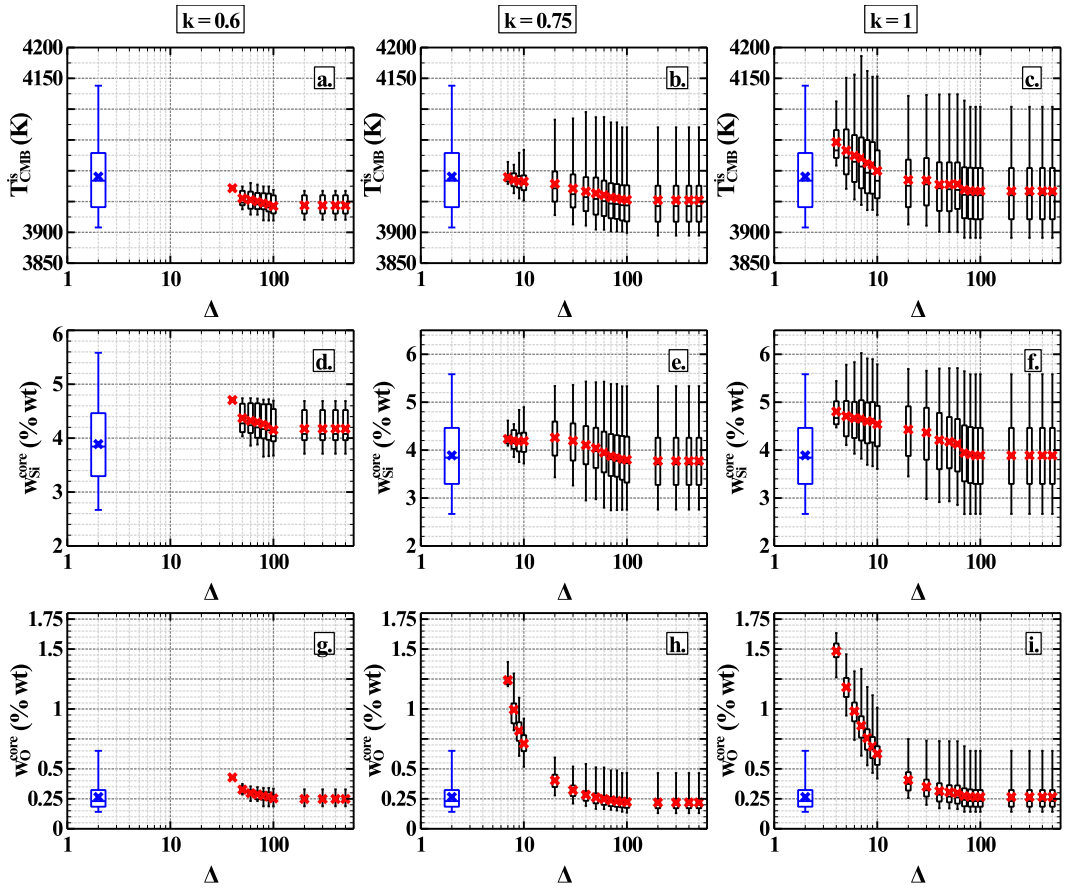

Figure 7. Effect of the silicate dilution Δ on the core properties (isentropic temperature at the CMB, light element content) for different values of k. First row, panels a. to c.: T^{is}_{CMB} in K. Second row, panels d. to f.: w^{core}_{Si} in % wt. Third row, panels g. to i.: w^{core}_{O} in % wt. The left, middle and right column shows the evolution of the parameters values for $k = 0.6$, $k = 0.75$ and $k = 1$, respectively. In each panel the entire solutions range are presented as boxplots, with the red cross being the mean value of the parameter, the white box delimiting the 1st and 3rd quartile, the horizontal line the median value and the vertical lines the minimum and maximum values. The reference model dataset is presented in blue with the same type of plot for comparison.

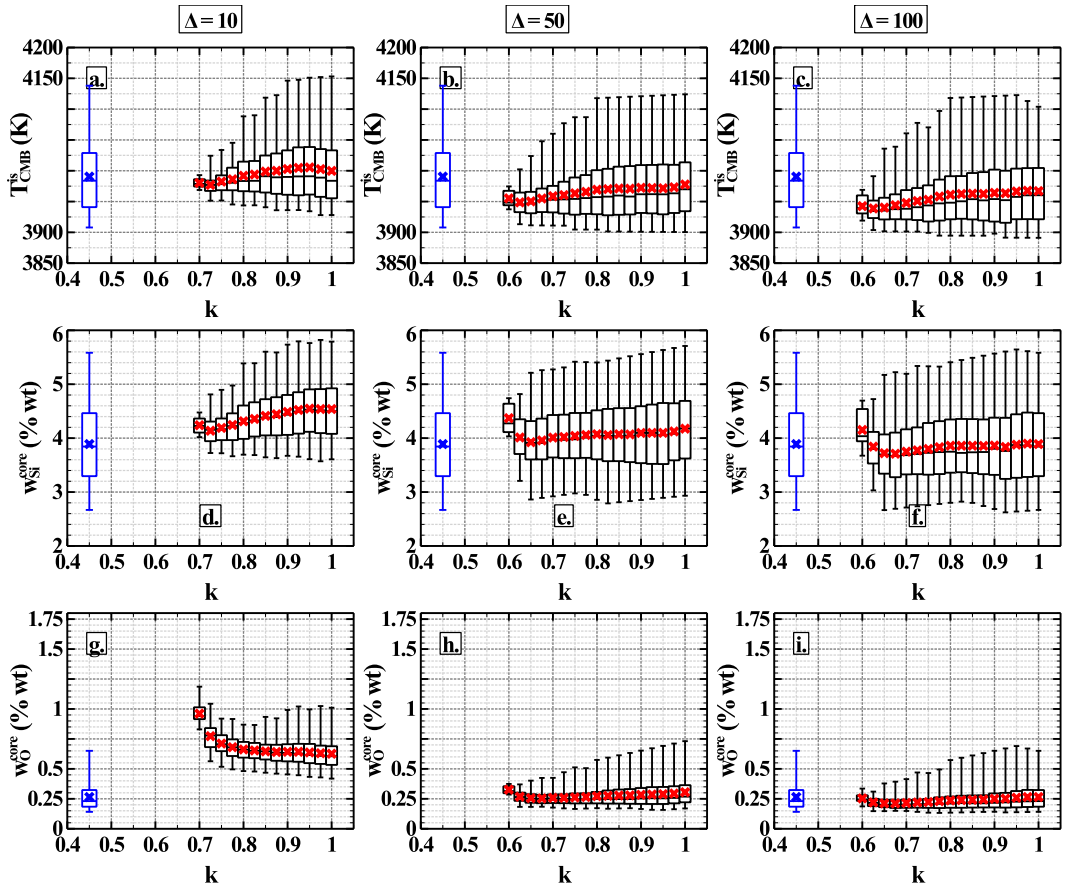

Figure 8. Effect of metal equilibrium k on the core properties (isentropic temperature at the CMB, light element content) for different values of Δ. First row, panels a. to c.: T^{is}_{CMB} in K. Second row, panels d. to f.: w^{core}_{Si} in % wt. Third row, panels g. to i.: w^{core}_{O} in % wt. The left, middle and right column shows the evolution of the parameters values for $\Delta = 10$, $\Delta = 50$ and $\Delta = 100$, respectively. In each panel the entire solutions range are presented as boxplots, with the red cross being the mean value of the parameter, the white box delimiting the 1st and 3rd quartile, the horizontal line the median value and the vertical lines the minimum and maximum values. The reference model dataset is presented in blue with the same type of plot for comparison.

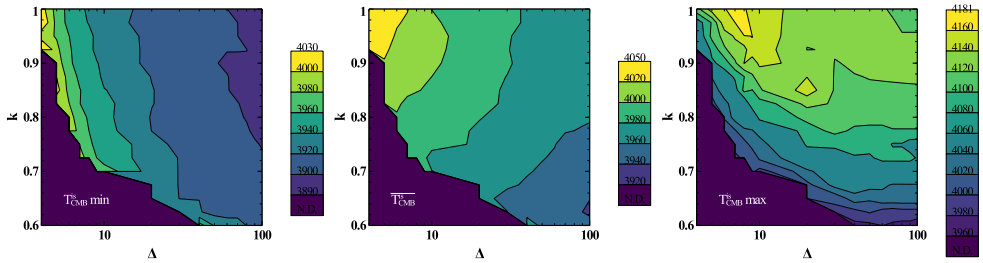

Figure 9. Evolution of minimum (left, $T^{is}_{CMB}min$), mean (center, $\overline{T^{is}_{CMB}}$) and maximum (right, $T^{is}_{CMB}max$) temperature at the CMB after isentropic mixing as a function of k (linear scale) and Δ (log scale). The color scale is changing from panel to panel to account for the different range of values (larger range for the maximum value, narrrower range for mean and minimum values).

T_x	a_x	b_x	c_x
T^{is}_{CMB} min	-63.92 $\pm$ 1.79	-58.77 $\pm$ 6.93	4065 $\pm$ 6.98
$\overline{T^{is}_{CMB}}$	-39.63 $\pm$ 0.74	78.46 $\pm$ 2.89	3970 $\pm$ 2.90
T^{is}_{CMB} max	25.46 $\pm$ 4	375 $\pm$ 15.86	3739 $\pm$

Table 2. Results of the fit for Equation 23 for different values of k. The logarithmic dependency of the different temperature on the Δ and k values is quite clear for the minimum and mean temperature, and less obvious for the maximum temperature.

indicating a lower sensitivity of Earth's core oxygen content to the metallic equilibrium than to the silicate equilibrium.

Most of the effect of k lies mostly in the range of possible output: as more metal equilibrates, it is possible to obtain different core compositions and heat contents and still be chemically coherent with the BSE. Indeed, the range of possible T^{is}_{CMB} values widen from a 50 K range (3920 to 3970 K) to a 230 K range (3891 to 4120 K) when k increases from 0.6 to 0.925 and $\Delta = 100$ (Figure 8, panel c.). This widening of the range of solutions is mostly borne by the higher temperature (and concomitantly higher Si and higher O) solutions rather than lower temperature solutions. This relates to the selection in input parameters presented in Figure 6: increasing the value of k allows for solution to happen for lower values of λ, thus increasing the average $\overline{P_{eq}}$ during accretion and consequently the values of T^{is}_{CMB}, w^{core}_{Si} and w^{core}_{O} are increased. Increasing the metallic equilibrium therefore allows for models with a steady increase of the magma ocean depth throughout accretion (lower values of λ) to yield chemically coherent models, those models yielding then higher temperatures for their cores. Decreasing the metallic equilibrium tends to select lower temperature solutions.

5 IMPLICATIONS FOR THE THERMAL AND DYNAMICAL HISTORY

5.1 Quantitative relationship between temperature and chemical equilibrium

Figure 9 shows that the values of CMB temperature decrease with the logarithm of Δ, an effect that is counterbalanced linearly when increasing the value of k. This effect is easier to see for $\overline{T^{is}_{CMB}}$ (middle panel Figure 9), with the highest value of $\overline{T^{is}_{CMB}}$ on the top left corner of the solution space (high k, low Δ) and the lowest values on the bottom right corner of the solution (low k, high Δ). Therefore it is possible to quantify the evolution of the primitive core temperature as a function of Δ and k. In Figure 9, we can summarize the effect of k and Δ to the following equation:

$$T_x = a_x log\Delta + b_x logk + c_x \tag{23}$$

where, T_x stands for the minimum, mean or maximum value of T^{is}_{CMB} and a_x, b_x and c_x are the fitted parameter (in K) for each temperature. The results of the fit are presented in Table 2. The core temperature dependency with the silicate dilution Δ is higher when most of the metal is equilibrated:. This is partly due to the lack of solutions, which tend to skew the value for higher Δ values, but is also an effect of the disequilibrium in the metal: as the k is lowered, the temperature. The values given in Table 2 can

yield a first approximation on the thermal state of the core for a given model is affected by disequilibrium. Indeed, most partitioning models assume equilibrium of the silicate on large scale (among other examples Rubie et al., 2011; Jacobson et al., 2017; Grewal et al., 2019; Suer et al., 2021; Loroch et al., 2024), due to fast convecting mantle silicate (Höink et al., 2006; Deguen et al., 2014) reacting with falling metallic spheres. These types of models will imply a lower temperature of the primitive core, thus favoring the cold core hypothesis of Nomura et al. (2014), Davies et al. (2015) or Dobrosavljevic et al. (2022) (CMB temperature of $\sim$ 3500 - 4000 K). Studies focusing on the Hf/W partitioning and the moon forming impact (Rudge et al., 2010; Nimmo et al., 2010; Fischer and Nimmo, 2018) tend to yield lower values of metal equilibrium, with values of $k \sim 0.3 - 0.6$, to account for the large size of the last impact. The value of $k = 0.3$ is also taken as a reference value for the sensitivity study of Gu et al. (2023). According to our results, these models will tend to favor also a cold core at the end of accretion: with $k = 0.6$ (higher end of the range proposed by Nimmo et al., 2010), the maximum temperature will be $\sim$ 4050 K for low silicate equilibrium ($\Delta \sim 4$) and $\sim$ 3950 K for full mantle equilibrium according to equation 23.

On the other hand, some models tend to favor hot core hypothesis for today's core, for instance Andrault et al. (2017) or Driscoll and Davies (2023) (CMB temperatures above 5000 K); and some models tends to favor higher core temperatures right after accretion, for instance King and Olson (2011) who proposed a mechanism allowing a higher intake of gravitational dissipation energy by the metallic phase, thus leading to a hot core right after accretion.

While the cold core hypothesis is easy to explain with classical accretion scenarios such as proposed in this paper, the hot core hypothesis necessitates more hypothesis: if we take the parameters in Table 2, and assume the temperature at the CMB after accretion is the same as the temperature estimated by Andrault et al. (2017, $T_{CMB} = 5000K$), for $k = 1$, no value of Δ can yield this temperature. The closest one are for Δ ranging from **6** and **50** to reach 4000 K at the CMB. Getting high temperatures by disequilibrium alone is therefore not possible, and necessitates other phenomena which can add more heat to the core: for instance gravitational dissipation energy intake (King and Olson, 2011; Clesi and Deguen, 2023), radiogenic element partitioning (Faure et al., 2020), or a combination of several mechanisms (Driscoll and Davies, 2023). However, what our results show, is that in order to obtain a hot core at the end of accretion, the amount of additional heat added to the core by these processes is lower if there is some chemical disequilibrium, yielding higher concentrations of light elements into the core.

5.2 Implications for dynamics of core formation and its modeling

5.2.1 Parameterization of the Reynolds number during core formation

The degree of disequilibrium between the silicate and metal is set by the dynamics of the falling metallic liquid within the liquid magma ocean (e.g. Deguen and Cardin, 2011; Rubie et al., 2003; Clesi et al., 2020; Qaddah et al., 2019). From our results, it is then possible to link the temperature of the core at the end of accretion to the dynamical regime of metal/silicate segregation, in particular the Reynolds number, which quantifies the ratio of inertial forces to the viscous forces in a moving fluid. To do so, we use the previous work of Clesi et al. (2020) and the following parameterization:

$$logR_c = a_{Re} logD_i + b_{Re} logRe + c_{Re} logR_\mu + d_{Re}, \tag{24}$$

where R_c is the ratio of equilibrated silicate over the total amount of silicate, D_i is the partitioning coefficient of element i, Re is the Reynolds number, R_μ the viscosity ratio of metal by silicate; and a_{Re}, b_{Re}, c_{Re} and d_{Re} constant fitted to the results.

The main control of the equilibrium rate, given by parameter R_c, are the partition coefficient and Reynolds number. By considering that the viscosity of metal and silicate are roughly the same, we get $R_\mu \sim 1$ and simplified this term in equation 24. To apply this parameterization to our system, it is also necessary to consider that $R_c = \frac{V_{eq}^{sil}}{V_{total}^{sil}} \simeq \frac{m_{eq}^{sil}}{m_{total}^{sil}}$, which is to say we consider that for a given step in accretion, the average density of the equilibrated silicate is the same as the average density of the magma ocean. Once these hypothesis are set, introducing equations 21 and 22 in equation 24 yields:

$$logRe = \frac{1}{b_{Re}} \left(log(\Delta k m_{total}^{met}) - log m_{eq}^{sil} - a_{Re} logD_i - d_{Re} \right). \tag{25}$$

Given the limitations of Clesi et al. (2020), especially the range of D_i values for which the parameterization is derived, then equation 25 can be applied for Ni and Co towards the end of accretion, especially the last

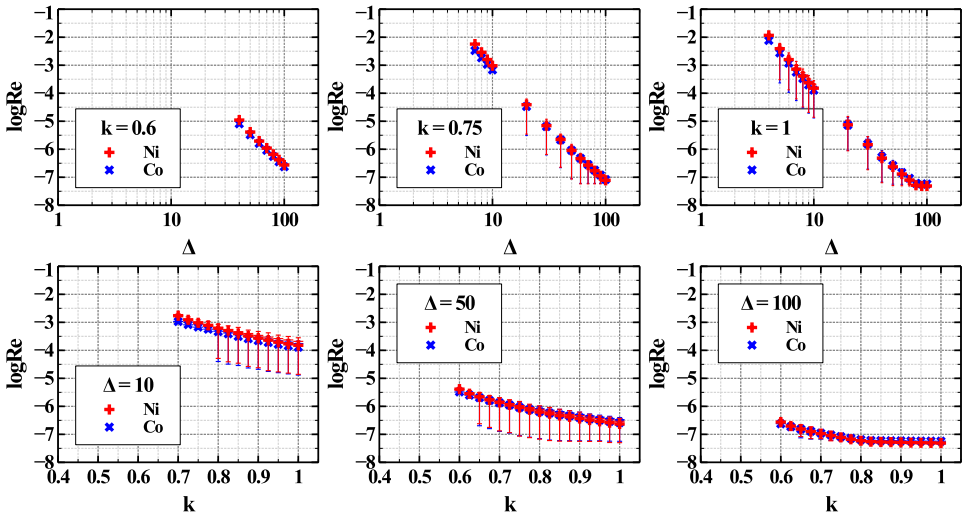

Figure 10. logRe during the accretion of the last 10% of the Earth's mass. First line as a function of the value Δ for fixed values of k, second line as a function of k for fixed values of Δ. The values of log Re are calculated for each solution using equation 25, with the values D_{Ni} and D_{Co} yielded by the model.

10% of mass accreted corresponding to the Moon-forming impact. The values of $logRe$ as a function of Δ and k when calculated with Ni and Co are presented in Figure 10. By construction of the parameterization, there is a linear relationship between logRe and k and Δ, showing that the higher the degree of equilibrium, the lower the Reynolds number needs to be. As shown in Figure 10, the variations in the Reynolds numbers are all in the range of laminar flow (i.e., the viscous forces are dominant compared to the inertial forces) but this range spans from very low ($Re \sim 10^{-7}$) to relatively higher values still in the viscous forces dominated regime ($Re \sim 10^{-2}$). In terms of fluid dynamics, this means that the more equilibrium is reached, the more stable the dynamic of metal/silicate segregation needs to be. Reciprocally, low degrees of equilibrium can be reached only if the dynamic tends towards more turbulent flows. These results are at odd with previous studies of the dynamics of metal-silicate segregation, which tend to favor turbulent fluid to reach equilibrium (Deguen and Cardin, 2011; Landeau et al., 2016; Samuel, 2012). This can be explained by the fact that Clesi et al. (2020) parameterization does not take into account the effect of diapir size, and thus select for non-turbulent flows. Keeping in mind this limitation, we can still nominally use the parameterization to try to infer the viscosity of the magma ocean for a given diapir size.

5.2.2 Implications for the viscosity of a magma ocean

Figure 10 shows that the dominant forces controlling the dynamics of core-mantle segregation during the last stages of accretion are the viscous forces. It is then possible to derive a range of plausible magma ocean viscosity for each particular equilibrium rate using the Reynolds number definition in this case:

$$Re = \frac{\rho_{silicate} R_{diapir} v_{diapir}}{\nu_{silicate}} \tag{26}$$

where $\rho_{silicate}$ is the average density of the magma ocean (kg.m^{-3}), R_{diapir} is the typical length of the metallic diapir (in m), v_{diapir} is the velocity of the diapir (in m.s^{-2}) and $\nu_{silicate}$ is the dynamic velocity in Pa.s. Given the range of Reynolds number given by equation 25 presented in Figure 10, the regime of diapir fall can be considered to be a Stokes flow, and therefore the velocity of the diapir is given by:

$$v_{diapir} = \frac{2}{9} \frac{(\rho_{metal} - \rho_{silicate}) g R_{diapir}^2}{\nu_{silicate}}, \tag{27}$$

where g is the gravitational acceleration of the accreting Earth (in m.s^{-2}) and ρ_{metal} the average density of the metal (in (kg.m^{-3}). It is then possible by combining equations 26 and 27 to have the following

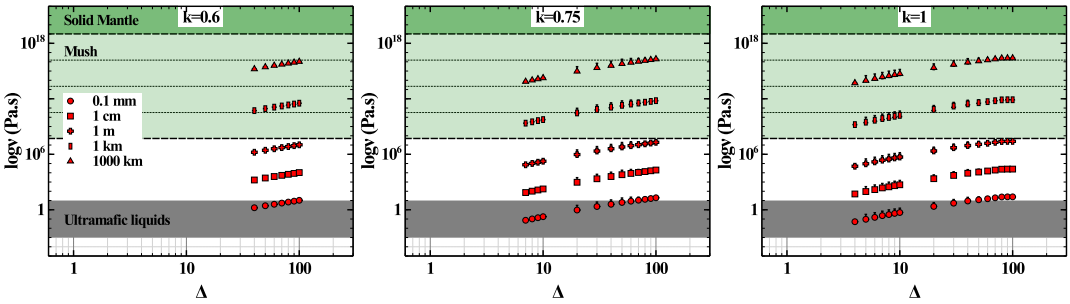

Figure 11. $logv$ as a function of Δ, for k = 0.6 (left panel), k=0.75 (middle panel) and k=1 (right panel), calculated with equation 28 from the values of $logRe$ shown in Figure 10, for different values of R_{diapir} (0.1 mm to 1000 km). The range of ultramafic to mafic melt viscosities is shown in grey. In dark green is figured the viscosity range of the solid mantle, with the lower value being 10^{18} Pa.s as used for the Moon in Michaut and Neufeld (2022). The light green area figures the range of mushy magma ocean defined by Solomatov (2007) for a melt volume fraction ranging from 0 to 1 (black dashed lines), with the dotted line marking the values for a volume melt fraction of 0.25, 0.5 and 0.75 (from top to bottom). All calculations shown here are made using the results obtained from Ni partitioning, as Ni and Co yielded similar results in Figure 10.

relationship for the viscosity of the silicate melt:

$$\nu_{silicate} = \left(\frac{2}{9} (\rho_{metal} - \rho_{silicate}) \rho_{silicate} g \frac{R_{diapir}^3}{Re} \right)^{1/2} . \tag{28}$$

By fixing different diapir sizes, it is then possible to use the results displayed in Figure 10 to obtain the viscosity of the magma ocean necessary to obtain the desired equilibrium rate. The results of the calculation are presented in Figure 11. As can be seen in Figure 11, the viscosity of ultramafic melts (here being defined by using the ranges given in Bajgain et al., 2022; Monteux et al., 2023; Huang et al., 2024; Russell et al., 2024, and references therein) explains our results only for very small diapir sizes (0.1 and 1 mm). In such a case, the thermal diffusion of the falling diapir becomes non-negligible, and the results presented in Figure 8 and 7 will be modified (see the supplementary materials of Clesi and Deguen, 2023). This also implies that even in the late stage of accretion, the impactor's core needs to be fully emulsified, even though equilibrium is not reached. Since these sizes of droplets are very unlikely during the last 10% of accretion, according to the simulations of the giant impact (Canup, 2004; Canup et al., 2023), then it is highly probable that the magma ocean viscosity during the late stages of accretion cannot be modeled by the viscosity of fully molten ultra-mafic melts, especially if water is present (Russell et al., 2024). In the case where the impactor core does not disintegrate and the diapir radius ranges between 100 to 1000 km, then the viscosity of the silicate is well represented by the mushy magma ocean model of (Solomatov, 2007), with the solid viscosity from Michaut and Neufeld (2022). This case is quite representative of the Moon-forming impact (Canup et al., 2023, and references therein), therefore the approximation of a fully molten magma ocean is wrong, especially at the end of accretion: a certain amount of crystals need to be presents to obtain some degree of equilibrium. Finally, the iron-rain scenario with centimeter- to meter-sized diapir yield viscosities of the magma ocean that are too high to be pure ultra-mafic melts, but too low to be included in the model of Solomatov (2007), even with a relatively low value for the solid end-member (10^{18} Pa.s, from Michaut and Neufeld, 2022, , which is a value for the Lunar mantle, but one order of magnitude below what is accepted for the Earth). This can mean two things: either the parameterization of Clesi et al. (2020) used here is wrong in its own range of validity, or the way we model magma ocean needs to be rethought. Indeed, there should not be a gap between the Solomatov (2007) model and the ultra-mafic liquids viscosities, unless (i) the magma ocean is not ultra-mafic, and therefore parameterizations of viscosity such as Russell et al. (2024) are useless in the context of planetary accretion; or (ii) the Solomatov (2007) exponential law using Mei et al. (2002) values needs to be updated to represent the primitive magma ocean.

Further studies are needed, in particular those studying the links between the chemical equilibrium and the dynamics of core/mantle segregation (see Landeau et al., 2021, for an example of such a study),

in particular for other elements than Ni and Co, as well of impactor sizes and compositions (one of the main limitations of Clesi et al., 2020). Moreover, further studies on the viscosity of silicate melts at high pressure covering more compositional and pressure range (which are the limitations of Huang et al., 2024; Russell et al., 2024, for instance) are needed to be able to quantify the degree of equilibrium necessary to obtain the Earth. Finally, further studies on the dynamics of mushy silicate liquids (e.g. Sen et al., 2023) will help decide if the approximation of a fully molten magma ocean is valid are not when modeling the accretion of the Earth.

6 CONCLUSIONS

To conclude, we used a previously developed method to quantify the effect of chemical disequilibrium on the thermal state of the core at the end of accretion. As the rate of equilibrium, in particular in the silicate, is decreased, the average pressure of equilibrium in the magma ocean needs to be increased to obtain a chemically coherent BSE. This increase in the average pressure of equilibrium translates directly into a higher initial core temperature. However, the maximum temperatures obtained from the minimum equilibrium rate ($T^{is}_{CMB} \sim 4200K$) is not enough to account for the hot core hypothesis, with 800 to 1000 K unaccounted for. Other mechanisms increasing the the core temperature are needed to produce a hot core.

When using a fixed equilibrium rate in the silicate, it is then possible to infer the dynamics of the metal/silicate segregation. If the magma ocean has the same viscosity as ultra-mafic melts (0.1-10 Pa.s), then it is necessary for the impactors' cores to be fully emulsified (millimetric to centimetric diapir sizes), even at the end of accretion. If one consider large diapirs, in particular at the end of accretion, then the magma ocean viscosity needs to be modeled as a mushy magma ocean, i.e. the fully molten hypothesis cannot be valid. Further studies are needed in order to fully comprehend the accretion process and the thermal evolution of the early core. In particular, the thermal model must be enhanced to account for more element and better equation of state for the metal (limitations developed in Clesi and Deguen, 2023). Moreover, the links between the dynamics of the metal/silicate segregation and the chemical equilibrium in a magma ocean needs to be accounted for more cases, with element and time dependency. Finally, further studies on the viscosity of mushy ultra-mafic melts are needed in order to properly model the dynamics of core formation.

ACKNOWLEDGMENTS

This work was supported by the European Research Council (ERC) under the European Unions Horizon 2020 research and innovation programme (grant number 716429). ISTerre is part of Labex OSUG@2020 (ANR10 LABX56). The authors declare no other sources of funding and no competing interest. The code used to produce the results presented here will be made available upon demand to the first author.

REFERENCES

Al'Tshuler, L., Brusnikin, S., and Kuz'Menkov, E. (1987). Isotherms and Grüneisen functions for 25 metals. *Journal of Applied Mechanics and Technical Physics*, 28(1):129–141.

Andrault, D., Bolfan-Casanova, N., Bouhifd, M., Boujibar, A., Garbarino, G., Manthilake, G., Mezouar, M., Monteux, J., Parisiades, P., and Pesce, G. (2017). Toward a coherent model for the melting behavior of the deep earth's mantle. *Physics of the Earth and Planetary Interiors*, 265:67–81.

Andrault, D., Bolfan-Casanova, N., Nigro, G. L., Bouhifd, M. A., Garbarino, G., and Mezouar, M. (2011). Solidus and liquidus profiles of chondritic mantle: Implication for melting of the Earth across its history. *Earth and planetary science letters*, 304(1-2):251–259.

Bajgain, S. K., Ashley, A. W., Mookherjee, M., Ghosh, D. B., and Karki, B. B. (2022). Insights into magma ocean dynamics from the transport properties of basaltic melt. *Nature communications*, 13(1):7590.

Birch, F. (1965). Energetics of core formation. *Journal of Geophysical research*, 70(24):6217–6221.

Bouhifd, M. and Jephcoat, A. (2011). Convergence of Ni and Co metal–silicate partition coefficients in the deep magma-ocean and coupled silicon–oxygen solubility in iron melts at high pressures. *Earth and Planetary Science Letters*, 307(3-4):341–348.

Bouhifd, M. A., Gautron, L., Bolfan-Casanova, N., Malavergne, V., Hammouda, T., Andrault, D., and Jephcoat, A. (2007). Potassium partitioning into molten iron alloys at high-pressure: Implications for Earth's core. *Physics of the Earth and Planetary Interiors*, 160(1):22–33.

Canup, R. M. (2004). Simulations of a late lunar-forming impact. *Icarus*, 168(2):433–456.
Canup, R. M., Righter, K., Dauphas, N., Pahlevan, K., Ćuk, M., Lock, S. J., Stewart, S. T., Salmon, J., Rufu, R., Nakajima, M., et al. (2023). Origin of the moon. *Reviews in Mineralogy and Geochemistry*, 89(1):53–102.
Clesi, V., Bouhifd, M., Bolfan-Casanova, N., Manthilake, G., Fabbrizio, A., and Andrault, D. (2016). Effect of H2O on metal–silicate partitioning of Ni, Co, V, Cr, Mn and Fe: Implications for the oxidation state of the Earth and Mars. *Geochimica et Cosmochimica Acta*, 192:97–121.
Clesi, V. and Deguen, R. (2023). Linking the core heat content to earth's accretion history. *Geochemistry, Geophysics, Geosystems*, 24(5):e2022GC010661.
Clesi, V. and Deguen, R. (2024a). Effect of discretization choices when modeling the thermo-chemical history of the accreting core. *Chemical Geology*, 657:122104.
Clesi, V. and Deguen, R. (2024b). Grüneisen parameter formalism in the study of the earth's core formation: a sensitivity study. *Geophysical Journal International*, 237(3):1275–1284.
Clesi, V., Monteux, J., Qaddah, B., Le Bars, M., Wacheul, J.-B., and Bouhifd, M. A. (2020). Dynamics of core-mantle separation: Influence of viscosity contrast and metal/silicate partition coefficients on the chemical equilibrium. *Physics of the Earth and Planetary Interiors*, 306:106547.
Davies, C., Pozzo, M., Gubbins, D., and Alfe, D. (2015). Constraints from material properties on the dynamics and evolution of earth's core. *Nature Geoscience*, 8(9):678–685.
Deguen, R. and Cardin, P. (2011). Thermochemical convection in Earth's inner core. *Geophysical Journal International*, 187(3):1101–1118.
Deguen, R., Landeau, M., and Olson, P. (2014). Turbulent metal–silicate mixing, fragmentation, and equilibration in magma oceans. *Earth and Planetary Science Letters*, 391:274–287.
Dobrosavljevic, V. V., Zhang, D., Sturhahn, W., Zhao, J., Toellner, T. S., Chariton, S., Prakapenka, V. B., Pardo, O. S., and Jackson, J. M. (2022). Melting and phase relations of fe-ni-si determined by a multi-technique approach. *Earth and Planetary Science Letters*, 584:117358.
Drake, M. J. and Righter, K. (2002). Determining the composition of the Earth. *Nature*, 416(6876):39–44.
Driscoll, P. and Davies, C. (2023). The "new core paradox:" challenges and potential solutions. *Journal of Geophysical Research: Solid Earth*, page e2022JB025355.
Dziewonski, A. M. and Anderson, D. L. (1981). Preliminary reference Earth model. *Physics of the earth and planetary interiors*, 25(4):297–356.
Faure, P., Bouhifd, M. A., Boyet, M., Manthilake, G., Clesi, V., and Devidal, J.-L. (2020). Uranium and thorium partitioning in the bulk silicate Earth and the oxygen content of Earth's core. *Geochimica et Cosmochimica Acta*, 275:83–98.
Fischer, R. A., Campbell, A. J., and Ciesla, F. J. (2017). Sensitivities of earth's core and mantle compositions to accretion and differentiation processes. *Earth and Planetary Science Letters*, 458:252–262.
Fischer, R. A., Nakajima, Y., Campbell, A. J., Frost, D. J., Harries, D., Langenhorst, F., Miyajima, N., Pollok, K., and Rubie, D. C. (2015). High pressure metal–silicate partitioning of Ni, Co, V, Cr, Si, and O. *Geochimica et Cosmochimica Acta*, 167:177–194.
Fischer, R. A. and Nimmo, F. (2018). Effects of core formation on the hf–w isotopic composition of the earth and dating of the moon-forming impact. *Earth and planetary science letters*, 499:257–265.
Frost, D. J., Asahara, Y., Rubie, D. C., Miyajima, N., Dubrovinsky, L. S., Holzapfel, C., Ohtani, E., Miyahara, M., and Sakai, T. (2010). Partitioning of oxygen between the Earth's mantle and core. *Journal of Geophysical Research: Solid Earth*, 115(B2).
Grewal, D. S., Dasgupta, R., Sun, C., Tsuno, K., and Costin, G. (2019). Delivery of carbon, nitrogen, and sulfur to the silicate Earth by a giant impact. *Science advances*, 5(1):eaau3669.
Gu, J. T., Fischer, R. A., Brennan, M. C., Clement, M. S., Jacobson, S. A., Kaib, N. A., O'Brien, D. P., and Raymond, S. N. (2023). Comparisons of the core and mantle compositions of earth analogs from different terrestrial planet formation scenarios. *Icarus*, 394:115425.
Höink, T., Schmalzl, J., and Hansen, U. (2006). Dynamics of metal-silicate separation in a terrestrial magma ocean. *Geochemistry, Geophysics, Geosystems*, 7(9).
Huang, D., Li, Y., and Murakami, M. (2024). Low viscosity of peridotite liquid: implications for magma ocean dynamics. *Geophysical Research Letters*, 51(7):e2023GL107608.
Izidoro, A., Bitsch, B., and Dasgupta, R. (2021). The effect of a strong pressure bump in the Sun's natal disk: terrestrial planet formation via planetesimal accretion rather than pebble accretion. *The*

Astrophysical Journal, 915(1):62.

Jacobson, S. A., Rubie, D. C., Hernlund, J., Morbidelli, A., and Nakajima, M. (2017). Formation, stratification, and mixing of the cores of Earth and Venus. *Earth and Planetary Science Letters*, 474:375–386.

King, C. and Olson, P. (2011). Heat partitioning in metal-silicate plumes during Earth differentiation. *Earth and Planetary Science Letters*, 304(3-4):577–586.

Landeau, M., Deguen, R., Phillips, D., Neufeld, J. A., Lherm, V., and Dalziel, S. B. (2021). Metal-silicate mixing by large Earth-forming impacts. *Earth and Planetary Science Letters*, 564:116888.

Landeau, M., Olson, P., Deguen, R., and Hirsh, B. H. (2016). Core merging and stratification following giant impact. *Nature Geoscience*, 9(10):786–789.

Loroch, D., Hackler, S., Rohrbach, A., Berndt, J., and Klemme, S. (2024). Accretion and core formation of earth-like planets: Insights from metal–silicate partitioning of siderophile and volatile elements. *Geosciences*, 14(11):281.

McDonough, W. and Sun, S.-S. (1995). The composition of the Earth. *Chemical geology*, 120(3-4):223–253.

Mei, S., Bai, W., Hiraga, T., and Kohlstedt, D. (2002). Influence of melt on the creep behavior of olivine–basalt aggregates under hydrous conditions. *Earth and Planetary Science Letters*, 201(3-4):491–507.

Michaut, C. and Neufeld, J. A. (2022). Formation of the lunar primary crust from a long-lived slushy magma ocean. *Geophysical Research Letters*, 49(2):e2021GL095408.

Monteux, J., Qaddah, B., and Andrault, D. (2023). Conditions for segregation of a crystal-rich layer within a convective magma ocean. *Journal of Geophysical Research: Planets*, 128(5):e2023JE007805.

Monteux, J., Ricard, Y., Coltice, N., Dubuffet, F., and Ulvrova, M. (2009). A model of metal–silicate separation on growing planets. *Earth and Planetary Science Letters*, 287(3-4):353–362.

Morbidelli, A., Chambers, J., Lunine, J., Petit, J.-M., Robert, F., Valsecchi, G., and Cyr, K. (2000). Source regions and timescales for the delivery of water to the Earth. *Meteoritics & Planetary Science*, 35(6):1309–1320.

Nimmo, F., O'brien, D., and Kleine, T. (2010). Tungsten isotopic evolution during late-stage accretion: constraints on earth–moon equilibration. *Earth and Planetary Science Letters*, 292(3-4):363–370.

Nomura, R., Hirose, K., Uesugi, K., Ohishi, Y., Tsuchiyama, A., Miyake, A., and Ueno, Y. (2014). Low core-mantle boundary temperature inferred from the solidus of pyrolite. *Science*, 343(6170):522–525.

Pu, C., Gao, X., Wu, Z., Du, Z., and Jing, Z. (2025). Metal-silicate partitioning of si, o, and mg at high pressures and high temperatures: Implications to the compositional evolution of core-forming metallic melts. *Geochemistry, Geophysics, Geosystems*, 26(2):e2024GC011940.

Qaddah, B., Monteux, J., Clesi, V., Bouhifd, M. A., and Le Bars, M. (2019). Dynamics and stability of an iron drop falling in a magma ocean. *Physics of the Earth and Planetary Interiors*, 289:75–89.

Raymond, S. N., O'Brien, D. P., Morbidelli, A., and Kaib, N. A. (2009). Building the terrestrial planets: Constrained accretion in the inner Solar System. *Icarus*, 203(2):644–662.

Rubie, D., Frost, D., Mann, U., Asahara, Y., Nimmo, F., Tsuno, K., Kegler, P., Holzheid, A., and Palme, H. (2011). Heterogeneous accretion, composition and core–mantle differentiation of the Earth. *Earth and Planetary Science Letters*, 301(1-2):31–42.

Rubie, D., Jacobson, S., Morbidelli, A., O'Brien, D., Young, E., de Vries, J., Nimmo, F., Palme, H., and Frost, D. (2015). Accretion and differentiation of the terrestrial planets with implications for the compositions of early-formed Solar System bodies and accretion of water. *Icarus*, 248:89–108.

Rubie, D., Melosh, H., Reid, J., Liebske, C., and Righter, K. (2003). Mechanisms of metal–silicate equilibration in the terrestrial magma ocean. *Earth and Planetary Science Letters*, 205(3-4):239–255.

Rudge, J. F., Kleine, T., and Bourdon, B. (2010). Broad bounds on earth's accretion and core formation constrained by geochemical models. *Nature Geoscience*, 3(6):439–443.

Russell, J. K., Hess, K.-U., and Dingwell, D. B. (2024). Ultramafic melt viscosity: a model. *Earth and Planetary Science Letters*, 643:118899.

Samuel, H. (2012). A re-evaluation of metal diapir breakup and equilibration in terrestrial magma oceans. *Earth and Planetary Science Letters*, 313:105–114.

Samuel, H., Tackley, P., and Evonuk, M. (2010). Heat partitioning in terrestrial planets during core formation by negative diapirism. *Earth and Planetary Science Letters*, 290(1-2):13–19.

Sen, J., Sarkar, S., and Mandal, N. (2023). Control of mush complex viscosity on mid-ocean ridge topography: A fluid–structure model analysis. *Physics of Fluids*, 35(6).

Siebert, J., Badro, J., Antonangeli, D., and Ryerson, F. J. (2012). Metal–silicate partitioning of Ni and Co in a deep magma ocean. *Earth and Planetary Science Letters*, 321:189–197.

Solomatov, V. (2007). Magma oceans and primordial mantle differentiation. *Evolution of the Earth*, 9:91–119.

Suer, T.-A., Siebert, J., Remusat, L., Day, J. M., Borensztajn, S., Doisneau, B., and Fiquet, G. (2021). Reconciling metal–silicate partitioning and late accretion in the earth. *Nature Communications*, 12(1):2913.

Ulvrová, M., Coltice, N., Ricard, Y., Labrosse, S., Dubuffet, F., Velímskỳ, J., and Šrámek, O. (2011). Compositional and thermal equilibration of particles, drops and diapirs in geophysical flows. *Geochemistry Geophysics Geosystems*, 12(10):1–11.

Wasson, J. T. and Kallemeyn, G. W. (1988). Compositions of chondrites. *Philosophical Transactions of the Royal Society of London. Series A, Mathematical and Physical Sciences*, 325(1587):535–544.

Wood, B., Wade, J., and Kilburn, M. (2008). Core formation and the oxidation state of the Earth: Additional constraints from Nb, V and Cr partitioning. *Geochimica et Cosmochimica Acta*, 72(5):1415–1426.

Zhang, D., Jackson, J. M., Zhao, J., Sturhahn, W., Alp, E. E., Hu, M. Y., Toellner, T. S., Murphy, C. A., and Prakapenka, V. B. (2016). Temperature of Earth's core constrained from melting of Fe and Fe0. 9Ni0. 1 at high pressures. *Earth and Planetary Science Letters*, 447:72–83.

Supplementary information to ”Effect of chemical disequilibrium during metal-silicate partitioning on the thermal state of the early core and implications on the dynamics of metal/silicate segregation”

Vincent Clesi[1,2] **and Renaud Deguen**[2,3]

[1]**Insitut für Mineralogie, Münster Universität, Correnstraße 24, 48149 Münster**
[2]**Univ Lyon, ENSL, UCBL, UJM, CNRS, LGL-TPE, F-69007 Lyon, France**
[3]**Univ. Grenoble Alpes, Univ. Savoie Mont Blanc, CNRS, IRD, Univ. Gustave Eiffel, ISTerre, 38000 Grenoble, France**

ABSTRACT

This is the supplementary figures for the paper entitled 'Effect of chemical disequilibrium during metal-silicate partitioning on the thermal state of the early core and implications on the dynamics of metal/silicate segregation'. Most of the figure are the final concentrations of each element in the mantle and the core (Fig. S4 to S19). Figures S1 to S3 are additions to the model description of section 3 in the main text.

Keywords: Accretion model, Core temperature, metal silicate partitioning

REFERENCES

Clesi, V. and Deguen, R. (2023). Linking the core heat content to earth's accretion history. *Geochemistry, Geophysics, Geosystems*, 24(5):e2022GC010661.

Clesi, V. and Deguen, R. (2024). Effect of discretization choices when modeling the thermo-chemical history of the accreting core. *Chemical Geology*, 657:122104.

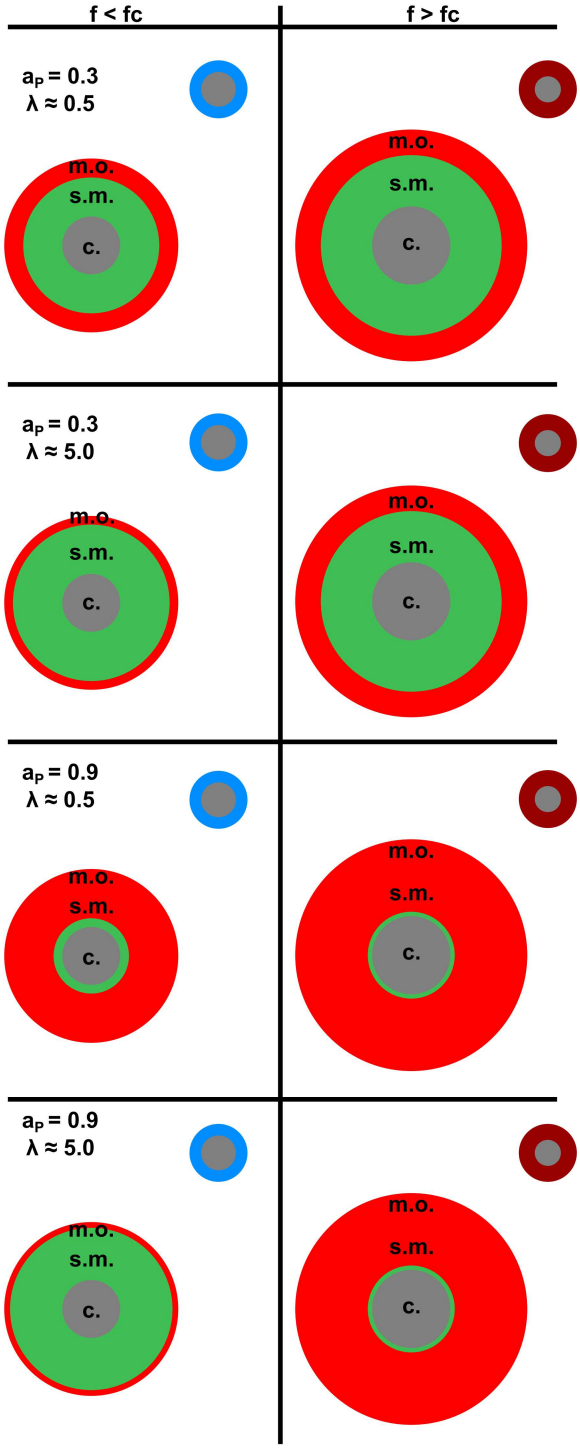

Figure S.1. Schematics of the physical meaning of the parameters a_P, f_c and λ used to parameterize the models of accretion. This Figure has been published in Clesi and Deguen (2024) and is reproduced here with the authorization of authors. The left columns shows the early part of accretion ($f < f_c$, more reduced impactor in blue). The right column hows the later stage of accretion ($f > f_c$, more oxidized impactor in dark red). The two first line shows the effect of λ for a low values of a_P on the depth of the magma ocean throughout accretion. The two bottom line shows the effect of λ for high value of a_P on the evolution of the depth of the magma ocean during accretion. m.o. = magma ocean (red), s.m. = solid mantle (green) and c. = core (grey).

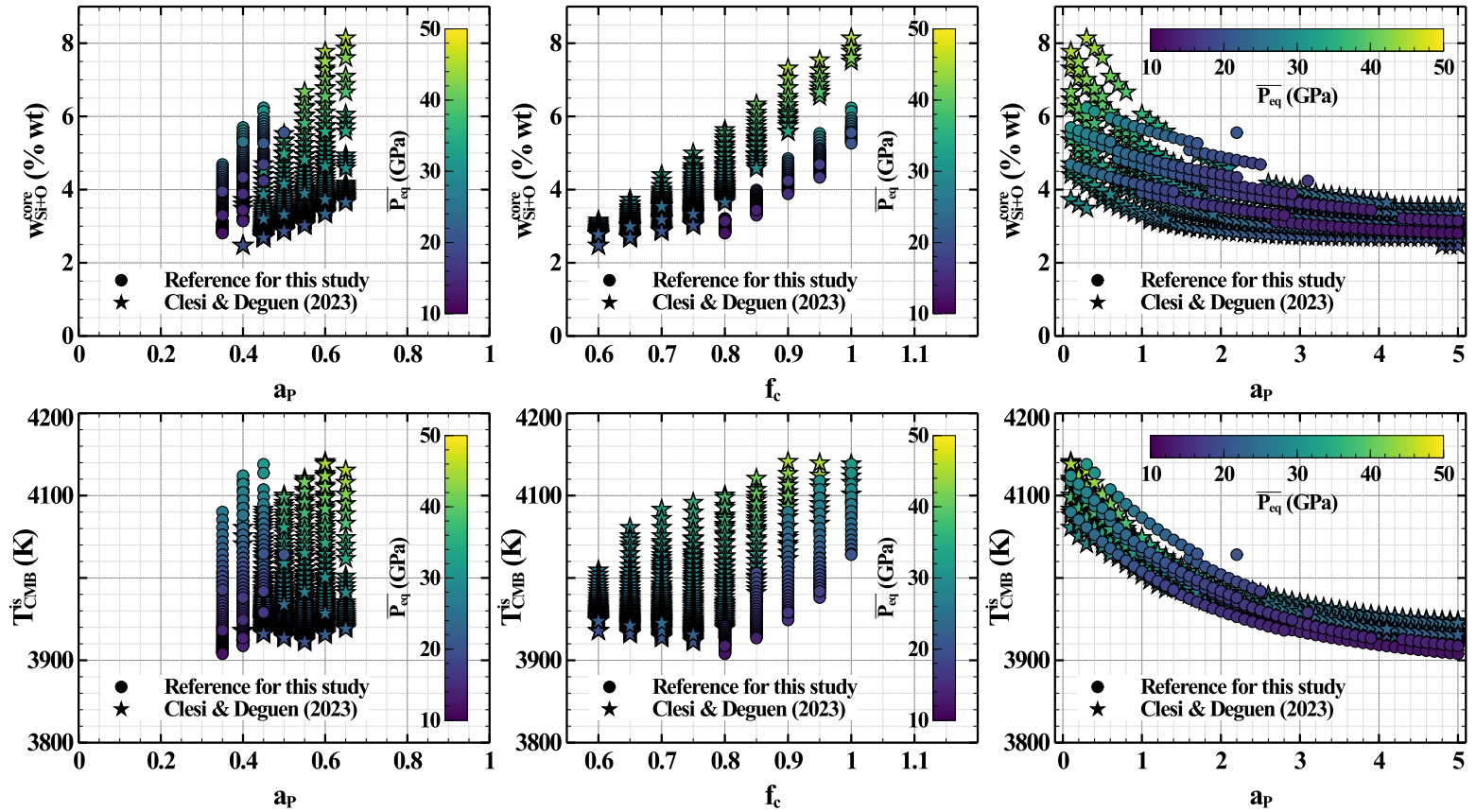

Figure S.2. Comparison of the reference solutions that are used in this study (round symbols) with the solutions obtained in Clesi and Deguen (2023) with another filter (stars). The format of this figure is the derived from Figure 8 of Clesi and Deguen (2023) to better highlight the differences between the solutions. The overall correlations are the same, with the weighted mean filter selecting for higher pressures models. The first row shows the correlation between light elements in the core with the three input parameters on each column: w^{core}_{Si+O} vs a_P on the left panel, w^{core}_{Si+O} vs f_c on the middle panel, w^{core}_{Si+O} vs λ on the right panel. The second row shows the correlation between the isentropic temperature at the CMB (T^{is}_{CMB} with the three input parameters presented in the same order. The color scale in all panel is the composite input parameter $\overline{P_{eq}}$ in GPa.

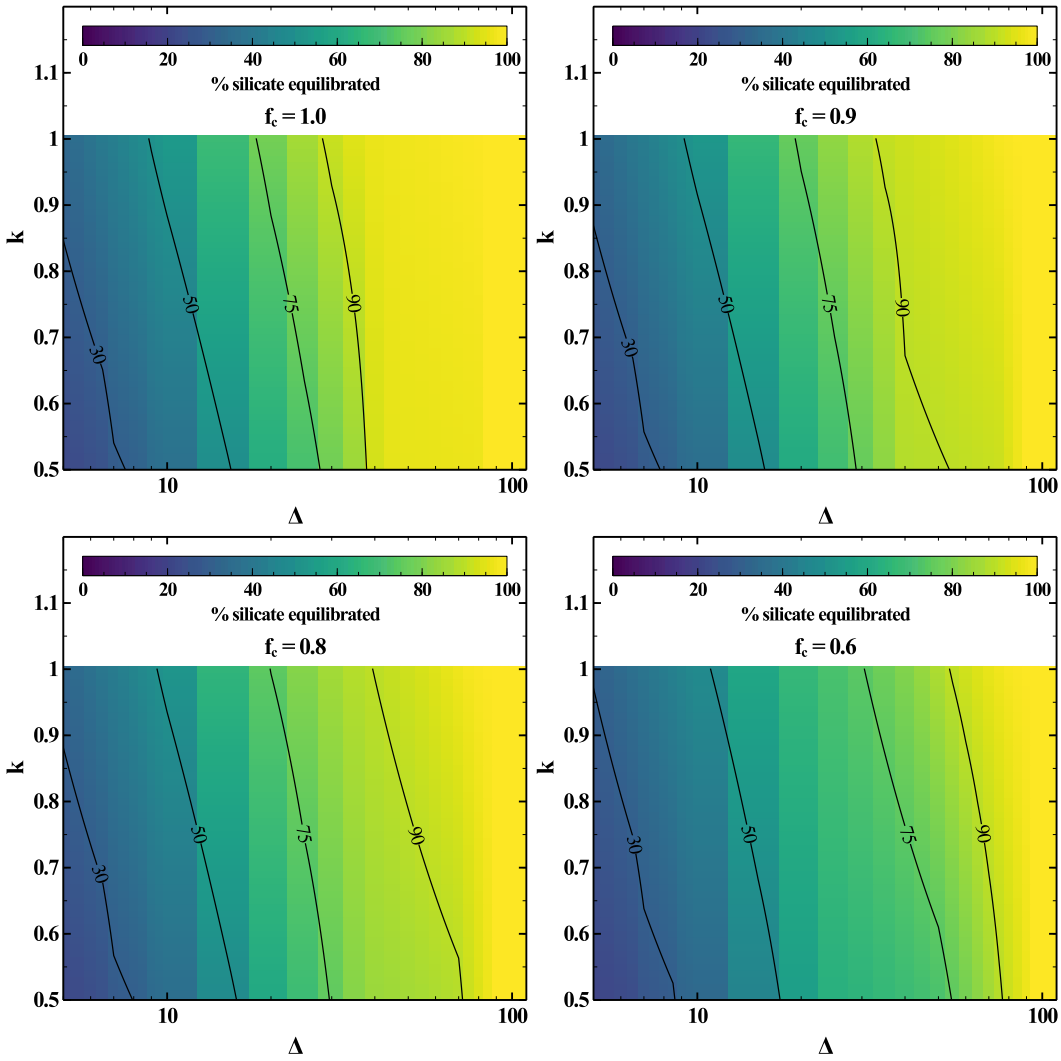

Figure S.3. Percentage of equilibrated mantle (color map) as a function of k (y-axis) and Δ (x-axis) for $f_c = 1$ (top left), $f_c = 0.9$ (top right), $f_c = 0.8$ (bottom left), $f_c = 0.8$ (bottom right). Full equilibrium is reached for $\Delta > 100$ in all relevant cases.

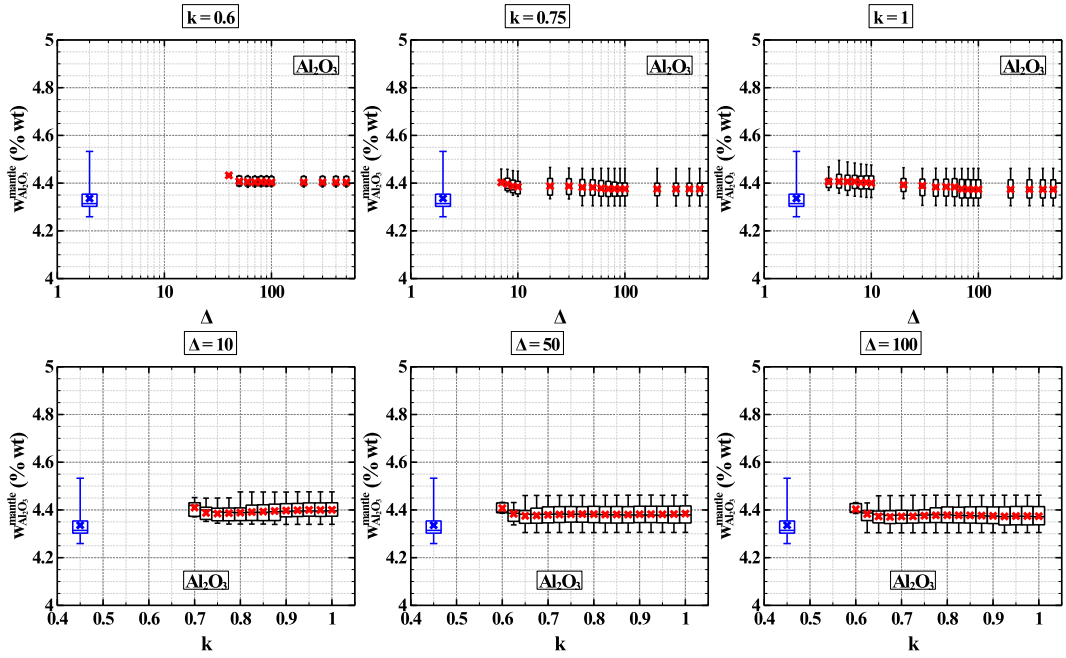

Figure S.4. Evolution of Al_2O_3 concentrations (% wt) in the mantle as a function of Δ for fixed values of k (top row), and as a function of k for fixed values of Δ (bottom row). In each panel the entire solutions range are presented as boxplots, with the red cross being the mean value of the parameter, the white box delimiting the 1st and 3rd quartile, the horizontal line the median value and the vertical lines the minimum and maximum values. The reference model dataset is presented in blue with the same type of plot for comparison.

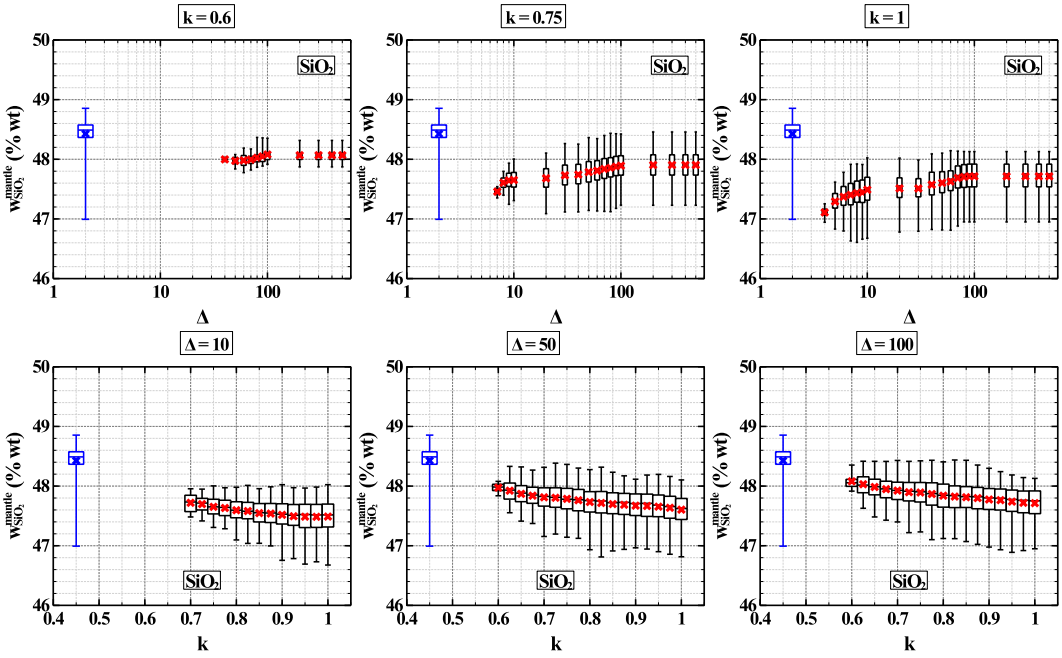

Figure S.5. Evolution of SiO_2 concentrations (% wt) in the mantle as a function of Δ for fixed values of k (top row), and as a function of k for fixed values of Δ (bottom row). In each panel the entire solutions range are presented as boxplots, with the red cross being the mean value of the parameter, the white box delimiting the 1st and 3rd quartile, the horizontal line the median value and the vertical lines the minimum and maximum values. The reference model dataset is presented in blue with the same type of plot for comparison.

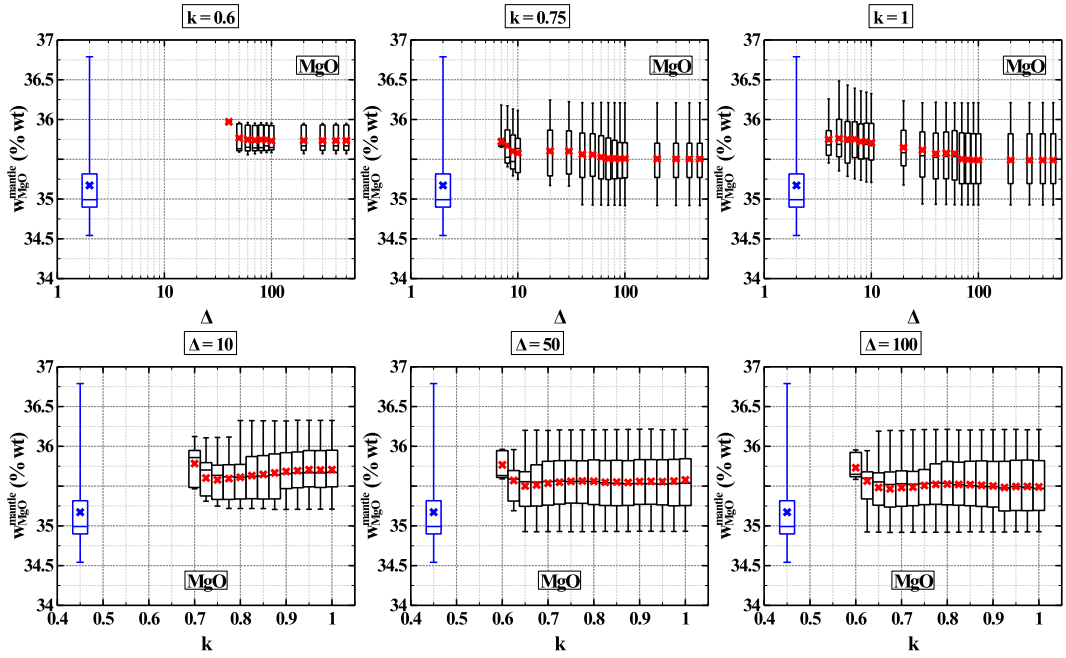

Figure S.6. Evolution of MgO concentrations (% wt) in the mantle as a function of Δ for fixed values of k (top row), and as a function of k for fixed values of Δ (bottom row). In each panel the entire solutions range are presented as boxplots, with the red cross being the mean value of the parameter, the white box delimiting the 1st and 3rd quartile, the horizontal line the median value and the vertical lines the minimum and maximum values. The reference model dataset is presented in blue with the same type of plot for comparison.

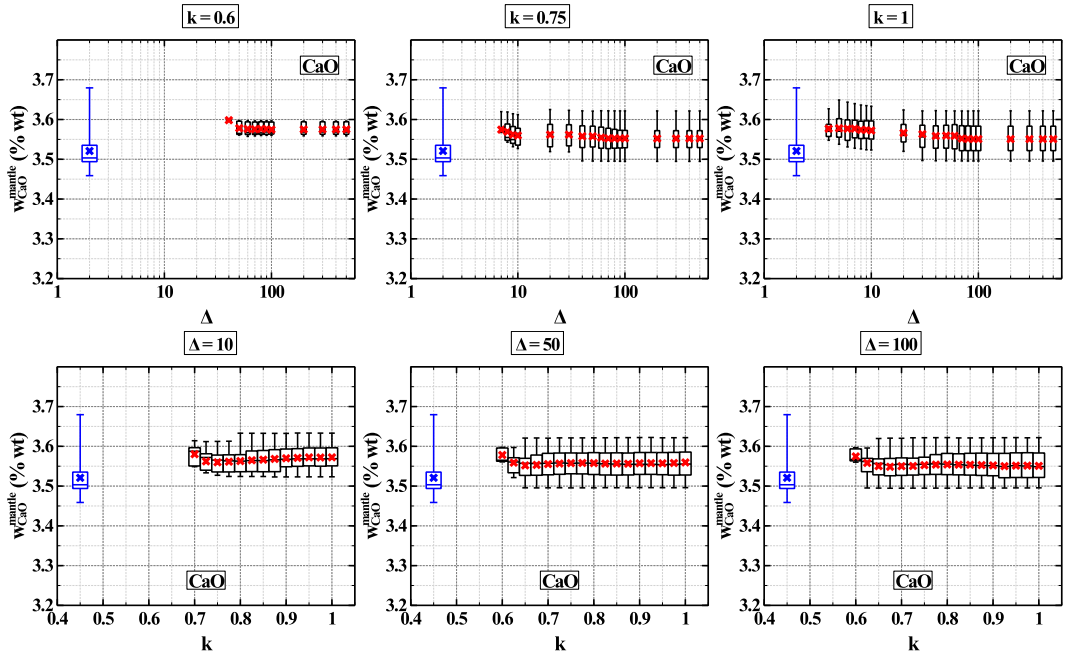

Figure S.7. Evolution of CaO concentrations (% wt) in the mantle as a function of Δ for fixed values of k (top row), and as a function of k for fixed values of Δ (bottom row). In each panel the entire solutions range are presented as boxplots, with the red cross being the mean value of the parameter, the white box delimiting the 1st and 3rd quartile, the horizontal line the median value and the vertical lines the minimum and maximum values. The reference model dataset is presented in blue with the same type of plot for comparison.

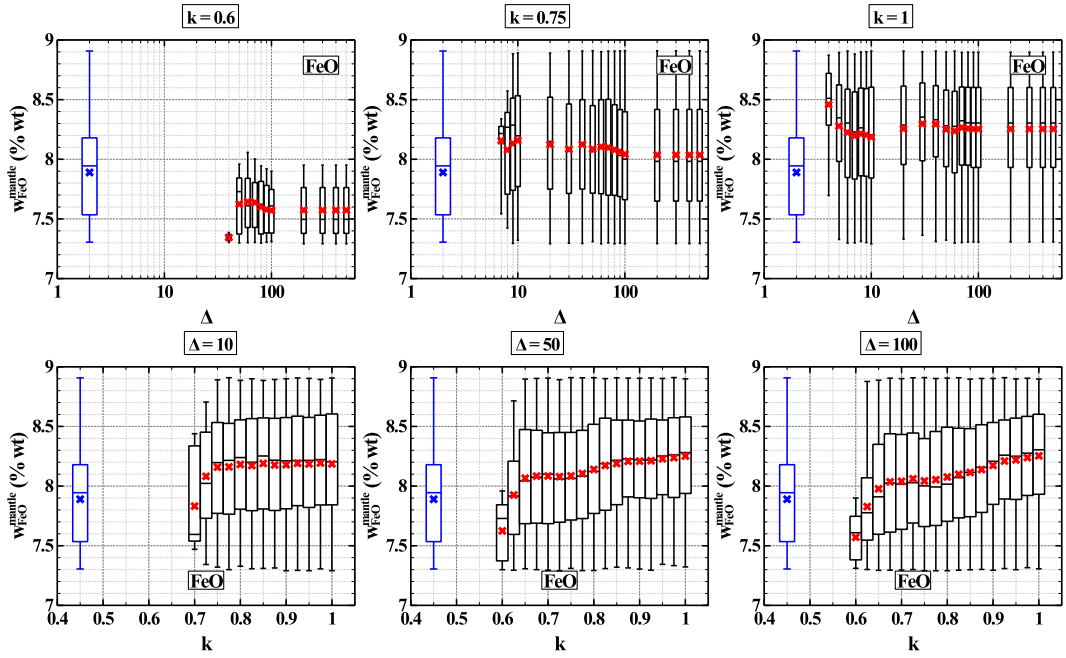

Figure S.8. Evolution of FeO concentrations (%wt) in the mantle as a function of Δ for fixed values of k (top row), and as a function of k for fixed values of Δ (bottom row). In each panel the entire solutions range are presented as boxplots, with the red cross being the mean value of the parameter, the white box delimiting the 1st and 3rd quartile, the horizontal line the median value and the vertical lines the minimum and maximum values. The reference model dataset is presented in blue with the same type of plot for comparison.

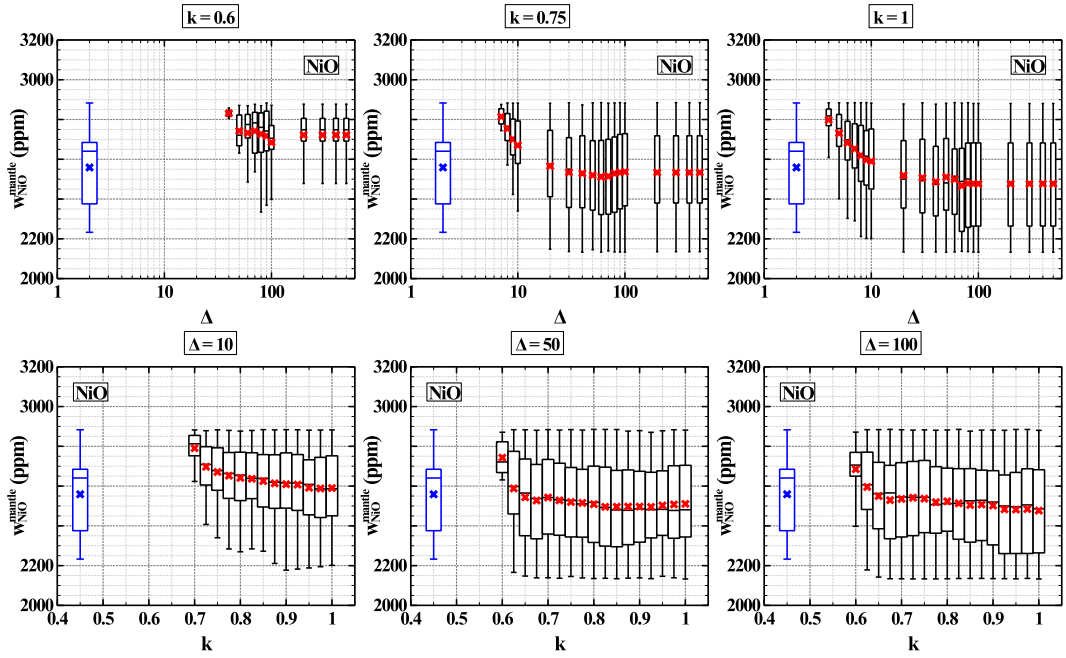

Figure S.9. Evolution of NiO concentrations (ppm) in the mantle as a function of Δ for fixed values of k (top row), and as a function of k for fixed values of Δ (bottom row). In each panel the entire solutions range are presented as boxplots, with the red cross being the mean value of the parameter, the white box delimiting the 1st and 3rd quartile, the horizontal line the median value and the vertical lines the minimum and maximum values. The reference model dataset is presented in blue with the same type of plot for comparison.

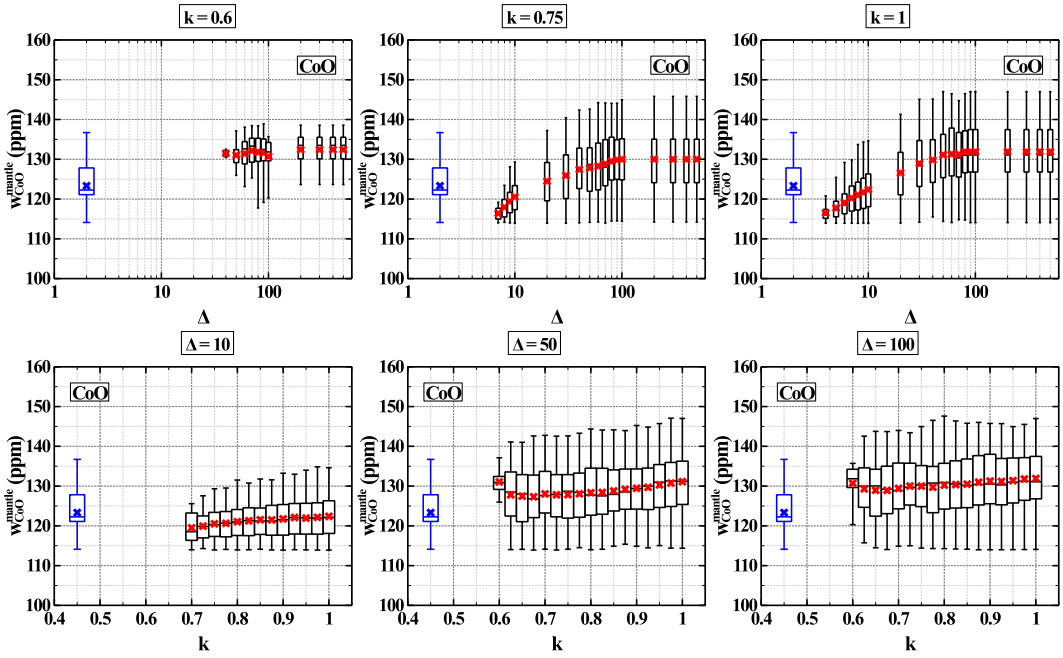

Figure S.10. Evolution of CoO concentrations (ppm) in the mantle as a function of Δ for fixed values of k (top row), and as a function of k for fixed values of Δ (bottom row). In each panel the entire solutions range are presented as boxplots, with the red cross being the mean value of the parameter, the white box delimiting the 1st and 3rd quartile, the horizontal line the median value and the vertical lines the minimum and maximum values. The reference model dataset is presented in blue with the same type of plot for comparison.

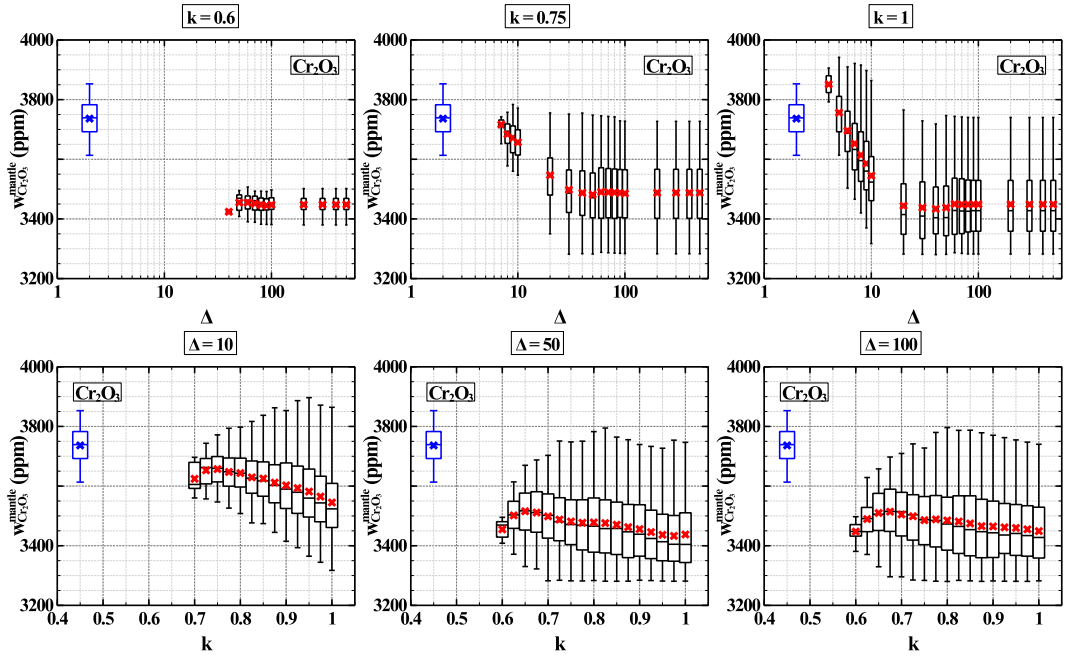

Figure S.11. Evolution of Cr_2O_3 concentrations (ppm) in the mantle as a function of Δ for fixed values of k (top row), and as a function of k for fixed values of Δ (bottom row). In each panel the entire solutions range are presented as boxplots, with the red cross being the mean value of the parameter, the white box delimiting the 1st and 3rd quartile, the horizontal line the median value and the vertical lines the minimum and maximum values. The reference model dataset is presented in blue with the same type of plot for comparison.

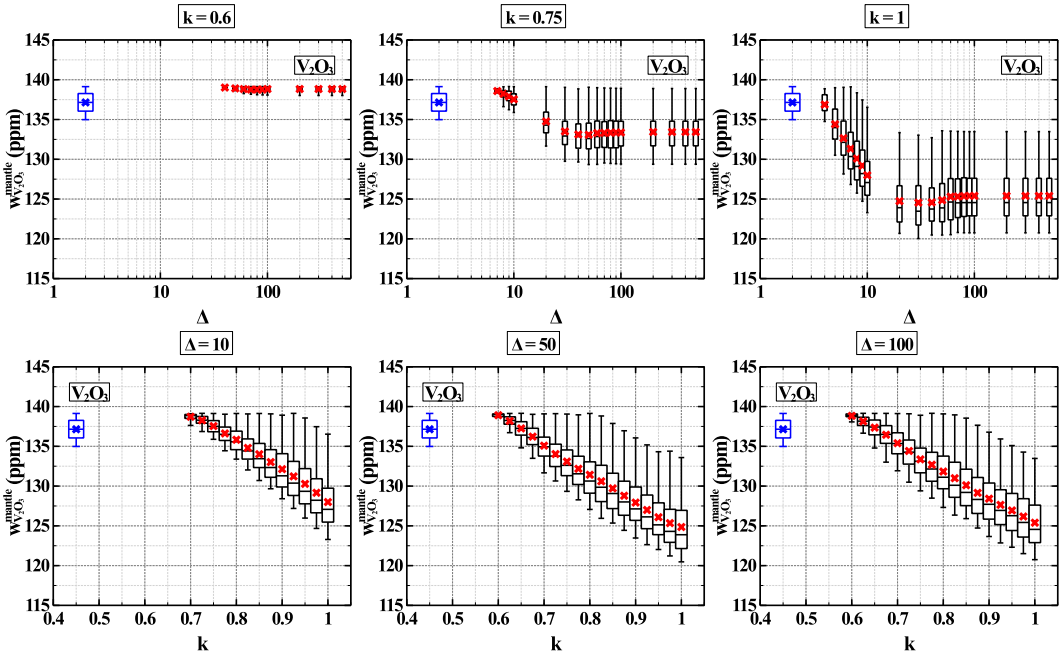

Figure S.12. Evolution of V_2O_3 concentrations (ppm) in the mantle as a function of Δ for fixed values of k (top row), and as a function of k for fixed values of Δ (bottom row). In each panel the entire solutions range are presented as boxplots, with the red cross being the mean value of the parameter, the white box delimiting the 1st and 3rd quartile, the horizontal line the median value and the vertical lines the minimum and maximum values. The reference model dataset is presented in blue with the same type of plot for comparison.

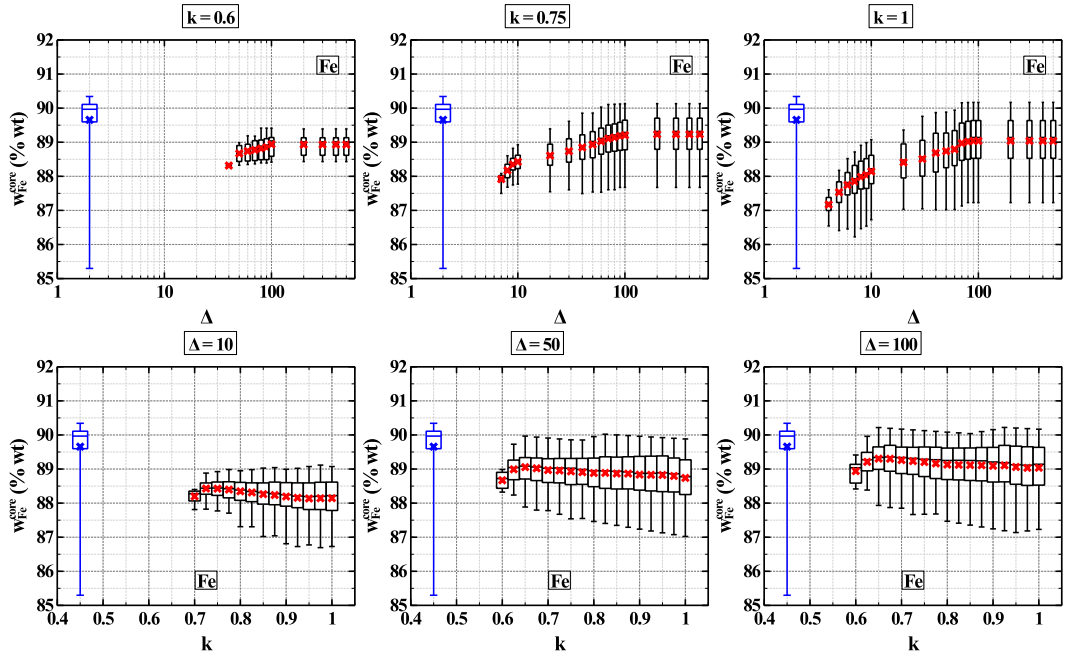

Figure S.13. Evolution of Fe concentrations (% wt) in the core as a function of Δ for fixed values of k (top row), and as a function of k for fixed values of Δ (bottom row). In each panel the entire solutions range are presented as boxplots, with the red cross being the mean value of the parameter, the white box delimiting the 1st and 3rd quartile, the horizontal line the median value and the vertical lines the minimum and maximum values. The reference model dataset is presented in blue with the same type of plot for comparison.

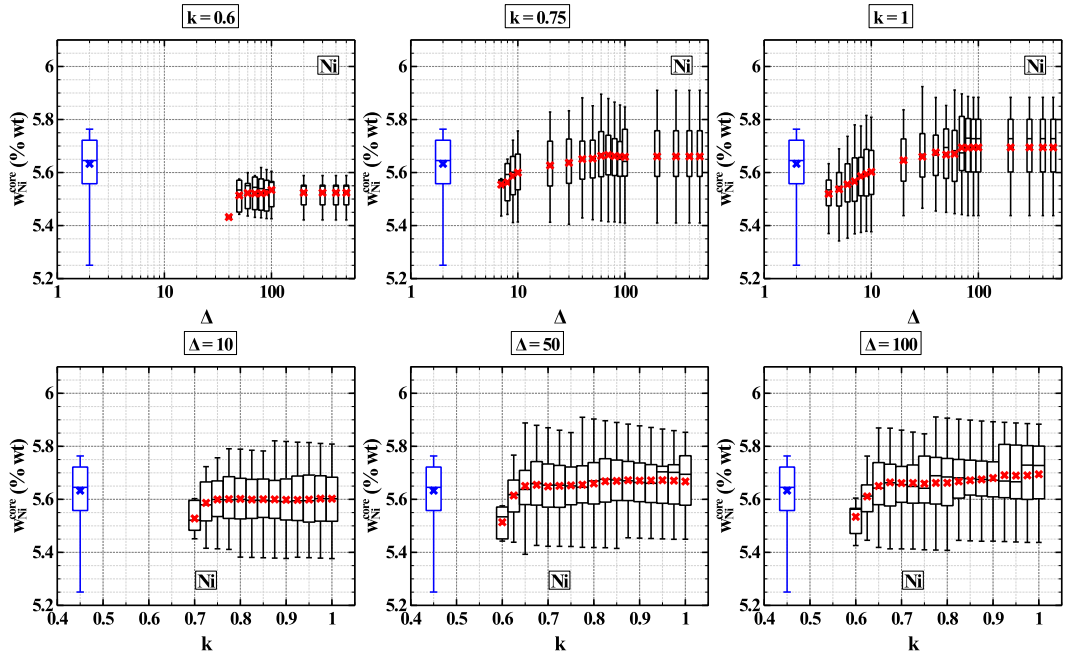

Figure S.14. Evolution of Ni concentrations (% wt) in the core as a function of Δ for fixed values of k (top row), and as a function of k for fixed values of Δ (bottom row). In each panel the entire solutions range are presented as boxplots, with the red cross being the mean value of the parameter, the white box delimiting the 1st and 3rd quartile, the horizontal line the median value and the vertical lines the minimum and maximum values. The reference model dataset is presented in blue with the same type of plot for comparison.

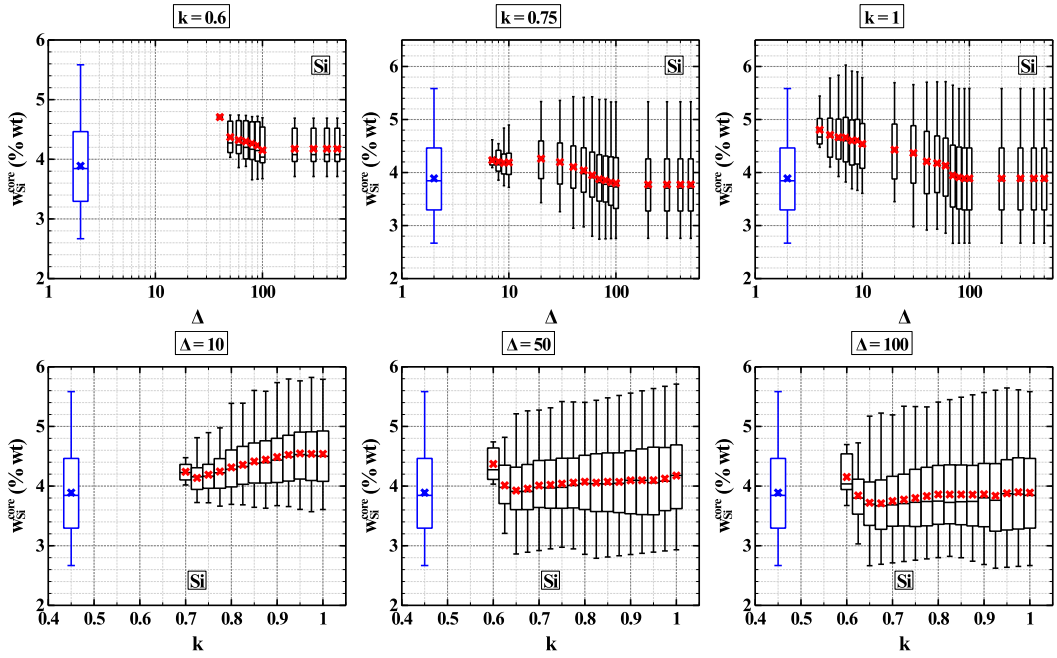

Figure S.15. Evolution of Si concentrations (% wt) in the core as a function of Δ for fixed values of k (top row), and as a function of k for fixed values of Δ (bottom row). In each panel the entire solutions range are presented as boxplots, with the red cross being the mean value of the parameter, the white box delimiting the 1st and 3rd quartile, the horizontal line the median value and the vertical lines the minimum and maximum values. The reference model dataset is presented in blue with the same type of plot for comparison.

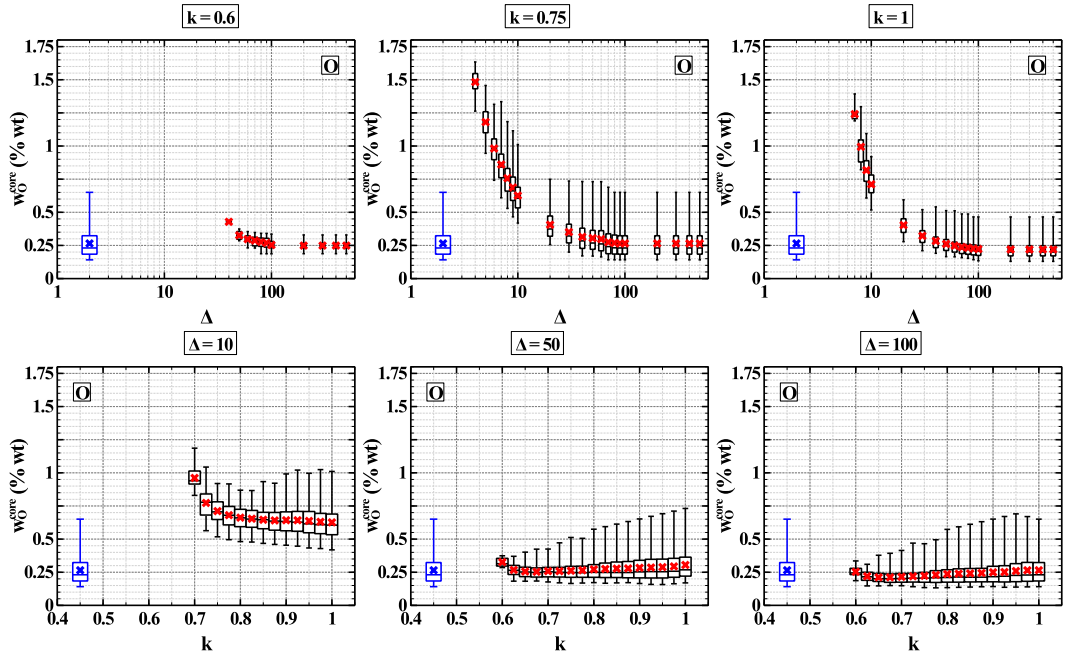

Figure S.16. Evolution of O concentrations (% wt) in the core as a function of Δ for fixed values of k (top row), and as a function of k for fixed values of Δ (bottom row). In each panel the entire solutions range are presented as boxplots, with the red cross being the mean value of the parameter, the white box delimiting the 1st and 3rd quartile, the horizontal line the median value and the vertical lines the minimum and maximum values. The reference model dataset is presented in blue with the same type of plot for comparison.

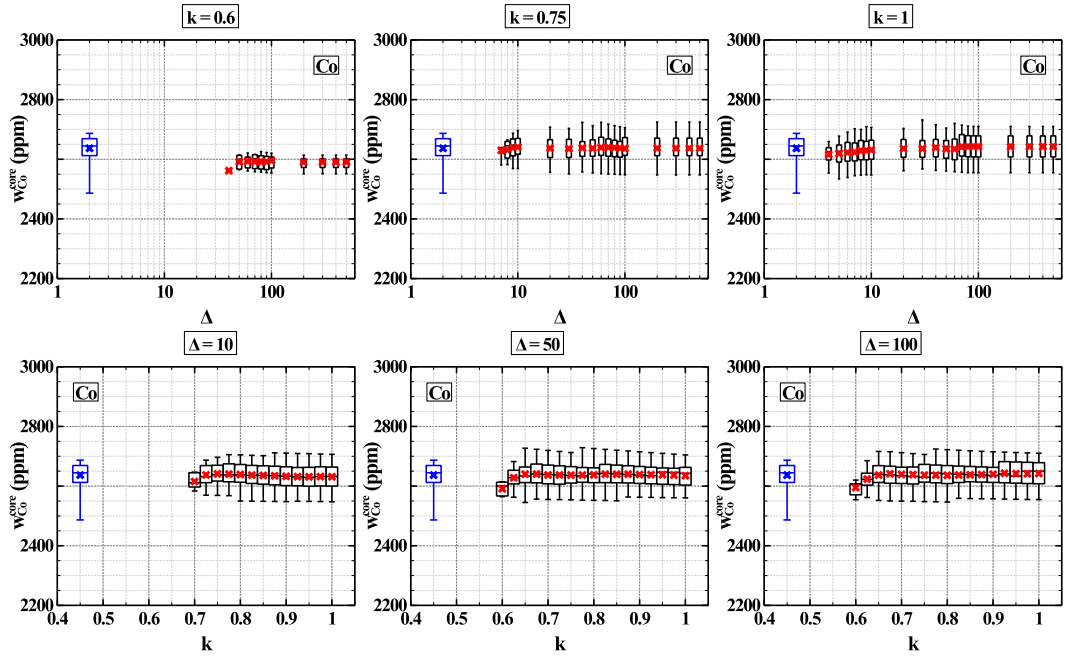

Figure S.17. Evolution of Co concentrations (ppm) in the core as a function of Δ for fixed values of k (top row), and as a function of k for fixed values of Δ (bottom row). In each panel the entire solutions range are presented as boxplots, with the red cross being the mean value of the parameter, the white box delimiting the 1st and 3rd quartile, the horizontal line the median value and the vertical lines the minimum and maximum values. The reference model dataset is presented in blue with the same type of plot for comparison.

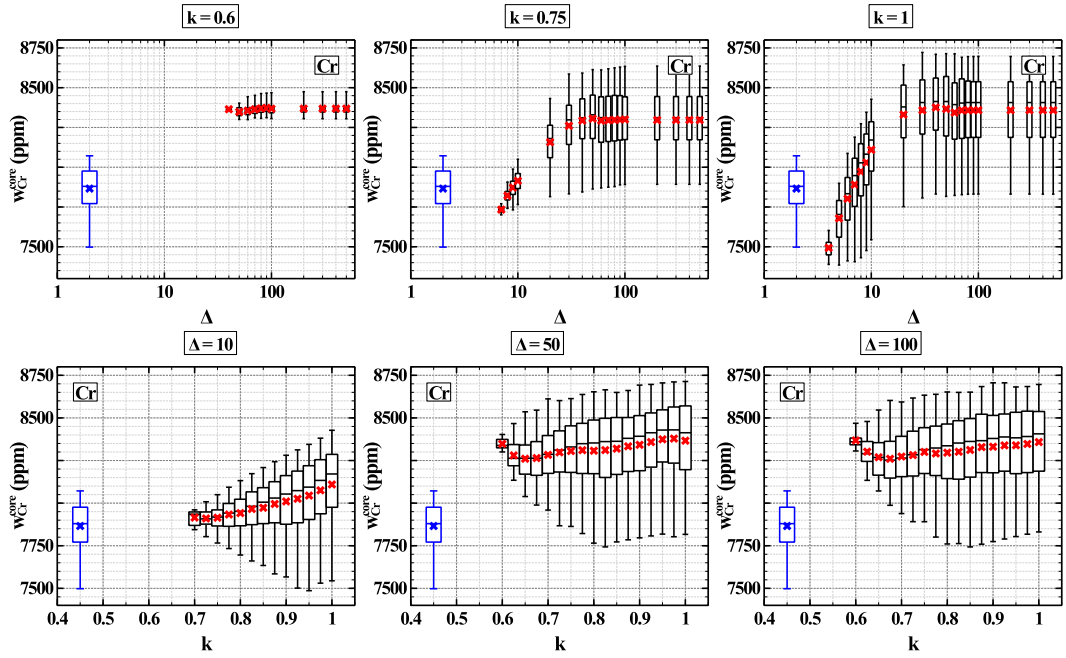

Figure S.18. Evolution of Cr concentrations (ppm) in the core as a function of Δ for fixed values of k (top row), and as a function of k for fixed values of Δ (bottom row). In each panel the entire solutions range are presented as boxplots, with the red cross being the mean value of the parameter, the white box delimiting the 1st and 3rd quartile, the horizontal line the median value and the vertical lines the minimum and maximum values. The reference model dataset is presented in blue with the same type of plot for comparison.

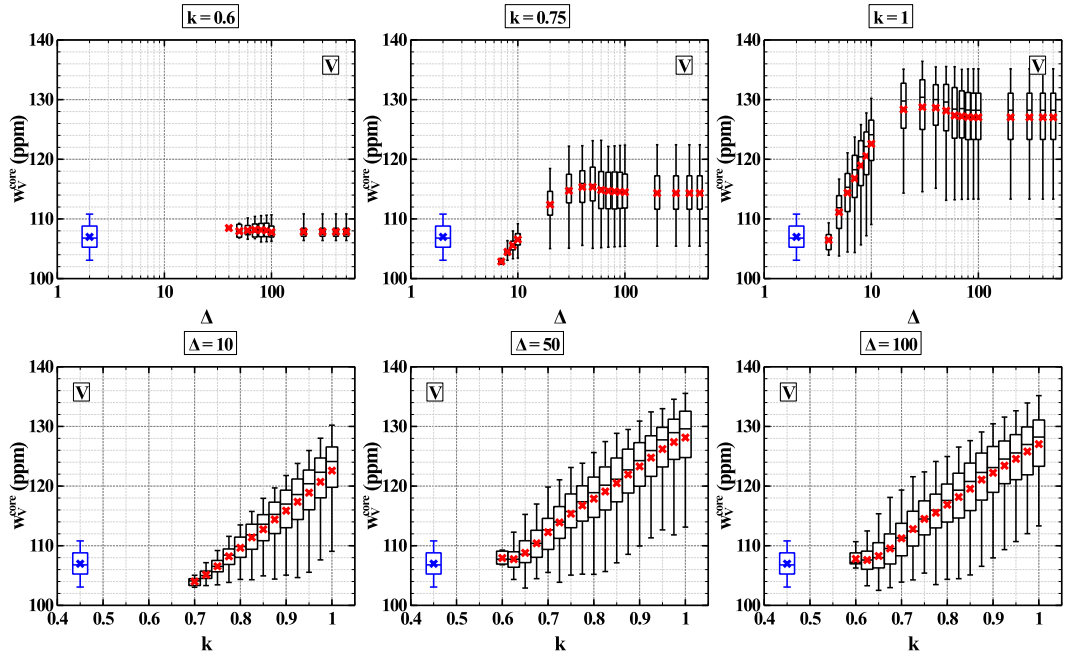

Figure S.19. Evolution of V concentrations (ppm) in the core as a function of Δ for fixed values of k (top row), and as a function of k for fixed values of Δ (bottom row). In each panel the entire solutions range are presented as boxplots, with the red cross being the mean value of the parameter, the white box delimiting the 1st and 3rd quartile, the horizontal line the median value and the vertical lines the minimum and maximum values. The reference model dataset is presented in blue with the same type of plot for comparison.